IEICE TRANSACTIONS

on Electronics

DOI:10.1587/transele.2024ECP5010

Publicized:2024/06/18

This advance publication article will be replaced by the finalized version after proofreading.

A PUBLICATION OF THE ELECTRONICS SOCIETY

The Institute of Electronics, Information and Communication Engineers
Kikai-Shinko-Kaikan Bldg., 5-8, Shibakoen 3chome, Minato-ku, TOKYO, 105-0011 JAPAN

PAPER

Scatterer Information Estimation Method by TD-SPT Using Numerical Data of Response Waveforms of Backward Transient Scattering Field Components

Keiji GOTO[†a)] **, Toru KAWANO**[†]**,** ***and*** **Ryohei NAKAMURA**[†]**,** ***Members***

SUMMARY This paper presents a scatterer information estimation method for both E- and H-polarizations based on a time-domain saddle-point technique (TD-SPT). The method utilizes numerical data of the response waveforms of the reflected geometric optical ray (RGO) series, which constitute the backward transient scattering field components when a line source and an observation point are at the same location. A scatterer selected in the paper is a two-dimensional (2-D) coated cylinder. The three types of scatterer information are the relative permittivity of a coating medium layer and its thickness, and the outer radius of a coated cylinder. Specifically, the scatterer information estimation formulas are derived by applying the TD-SPT represented in RGO series to the amplitude intensity ratios (AIRs) of adjacent RGO components. By focusing on the analytical results that the AIRs are independent of polarization, we analytically clarify that all the estimation formulas derived here denote polarization independence. The estimates are obtained by substituting numerical data of the peaks of the response waveforms of the RGO components and their arrival times, as well as numerical parameters of a pulse source, into the estimation formulas and performing iterative calculations. We derive approximations to the estimation errors that are useful in quantitatively evaluating the errors of the estimates. The effectiveness of the scatterer information estimation method is substantiated by comparing the estimates with the set values. The polarization independence of the estimation formulas is validated numerically by contrasting the estimates for E- and H-polarizations. The estimation errors are discussed using the approximations to the errors of the estimates when a line source and an observation point are at the same location. Thereafter, the discrepancies that arise between the estimation errors when a line source and an observation point are at different locations are discussed. The methods to control the estimation accuracy and the computational time are also discussed.

key words: *scatterer information estimation method, time-domain saddle-point technique (TD-SPT), polarization independence of estimation formulas, backward transient scattering field components, amplitude intensity ratios (AIRs)*

1. Introduction

One of the canonical problems of high-frequency (HF) electromagnetic (EM) wave scattering [1]-[4] includes the scattering problems by two-dimensional (2-D) cylindrical objects [3]-[19]. The 2-D cylindrical objects are classified according to their materials and structures as metal cylinders [5]-[7], [10], [14], dielectric cylinders [13], [15], and metal cylinders coated with a dielectric medium (coated cylinders) [8], [9], [11], [12], [16]-[19]. The analysis methods of EM wave scattering from 2-D cylindrical objects can be broadly classified into two categories: frequency-domain (FD) analysis [5]-[11], [13]-[16] and time-domain (TD) analysis [12], [15], [17]-[19].

The estimation of non-destructive deterioration diagnosis of reinforced concrete structures using ultra-wideband (UWB) pulse waves [20], as an application of TD analysis of EM wave scattering by 2-D coated cylinders, has recently become an important research topic [17]-[19]. Nishimoto *et al*. constructed a model of a corroded rebar in reinforced concrete as a 2-D coated cylinder and irradiated it with UWB pulse waves to investigate the relationship between the response waveforms and the corrosion states [18]. It has been reported that, with the exception of the initial stage of corrosion, it is possible to estimate the corrosion state of the rebar by examining the changes in the response waveform [19].

The authors have developed several asymptotic solutions for the HF transient scattering field from coated cylinders. These include a TD asymptotic-numerical solution (TD-ANS) [21], [22], a TD saddle-point technique (TD-SPT) [23], [24], and a TD Fourier transform method (TD-FTM) [25], [26]. The aforementioned HF asymptotic solutions for a backward transient scattering field when a line source and an observation point are at different locations are represented by a superposition of a direct geometric optical ray (DGO) and a reflected geometric optical ray (RGO) series [22]-[26].

Transient scattering response waveforms contain information regarding the structure, dimensions, and material of a scatterer. The authors proposed a scatterer information estimation method using numerical data of the response waveforms of both the DGO and the RGO series, which are the backward transient scattering field components from a 2-D coated cylinder when a line source and an observation point are located at different positions [27]. This method combines the interpretation method for the inversion phenomena of response waveforms [23] with that for the amplitude intensities of response waveforms [26].

† The authors are with The National Defense Academy of Japan, Yokosuka-shi, 239-8686 Japan.
a) E-mail: keigoto@nda.ac.jp

We derived the minimum thickness of a coating medium layer for which the estimation method is valid and proposed the applicable conditions of the estimation method. Furthermore, we numerically confirmed the polarization independence of the estimation formulas.

Conversely, when a line source and an observation point are at the same location, there is no DGO component and only the RGO series reaches the observation point (see Fig. 2). Consequently, the estimation formulas for the relative permittivity of a surrounding medium (see (11) in [27]) and the outer radius of a coated cylinder (see (20) in [27]) cannot be derived, as there is no DGO. Therefore, in the case of backward transient scattering, where a line source and an observation point are at the same location, the scatterer information estimation method proposed in Section 4.3 of [27] is not applicable. Furthermore, the analytical study of the polarization independence of the estimation formulas used in the estimation method is not covered in [27].

With this research background, this paper presents a scatterer information estimation method by TD-SPT using numerical data of the response waveforms of the RGO series that constitute the backward transient scattering field components when a line source and an observation point are at the same location [28], [29]. A 2-D coated cylinder is selected as a scatterer, and the thickness of a coating medium layer is assumed to satisfy the applicable condition of the estimation method [27], [29].

Specifically, we propose a scatterer information estimation method for both E- and H-polarizations, where the electric and magnetic field components of an incident pulse wave are assumed to be perpendicular to the incident plane, respectively. The three types of scatterer information are the relative permittivity of a coating medium layer and its thickness, and the outer radius of a coated cylinder. The application of the TD-SPT represented in the RGO series to the amplitude intensity ratios (AIRs) of the adjacent RGO components yields the estimation formulas for scatterer information. By focusing on the analytical results that the AIRs are independent of polarization, we will analytically clarify that the estimation formulas of scatterer information denote the polarization independence. The estimates are obtained by substituting numerical data of the peaks of the response waveforms of the RGO components and their arrival times, and the numerical parameters of a pulse source into the estimation formulas and performing iterative calculations. We derive approximations to the estimation errors that are useful in quantitatively evaluating the accuracy of the estimates obtained by the estimation method.

The effectiveness of the scatterer information estimation method is clarified by comparing the estimates with the set values. The polarization independence of the estimation formulas is validated numerically by contrasting the estimates for E- and H-polarizations. We calculate the estimation errors using the approximations to the errors of the estimates when a line source and an observation point are at the same location, and then discuss the discrepancies that arise between the estimation errors when a line source and an observation point are at different locations which is shown in [27]. The methods to control the estimation accuracy and the computation time are also discussed.

The time dependence $\exp(-i\omega t)$ is assumed but suppressed throughout the text.

2. Formulation

Figure 1 shows a cross-sectional geometry of a 2-D coated cylinder with an outer radius of $\rho = a\ (= b + h)$. The cylinder is a metal cylinder with an inner radius of $\rho = b$, coated with a coating medium 2 (ε_2, μ_0) of thickness $h\ (= a - b)$. The coordinate systems (x, y, z) and (ρ, ϕ) are employed. The permittivity ε_2 of medium 2 is defined by $\varepsilon_2 = \varepsilon_0 \varepsilon_{2r}$, where ε_{2r} is a relative permittivity of medium 2. The constitutive parameters ε_0 and μ_0 are a permittivity and a permeability in free space, respectively. An electric or magnetic line source $\mathrm{Q}(\rho_0, \phi_0)$ is placed parallel to the central axis of a coated cylinder in a surrounding medium 1 (ε_1, μ_0). The permittivity ε_1 of medium 1 is defined by $\varepsilon_1 = \varepsilon_0 \varepsilon_{1r}$, where ε_{1r} is the relative permittivity of medium 1. An observation point $\mathrm{P}(\rho, \phi)$ in medium 1 is placed at the same location as the line source Q. It is assumed that the permittivities of medium 1 and medium 2 are lossless and that $\varepsilon_{1r} < \varepsilon_{2r}$. Furthermore, it is assumed that the thickness h of a coating medium layer is greater than or equal to the minimum thickness h_c $(h \geq h_c)$, which satisfies the applicable condition of the scatterer information estimation method (see (A·3) in Appendix A) [27], [29].

Figure 2 shows the propagation paths of backward transient scattering waves (⟶: solid curve with arrow), in which a cylindrical pulse wave is radiated from a line source Q and incident perpendicularly on a coated cylinder. The wave then arrives at an observation point P. Since the points Q and P are at the same location, there is no DGO, and the RGO series components ($\mathrm{RGO}_p, p = 0, 1, \cdots, M_j$, $j = \mathrm{E}, \mathrm{H}$ see Appendix B) reach the point P. The symbol M_j represents the number of truncated terms in the RGO

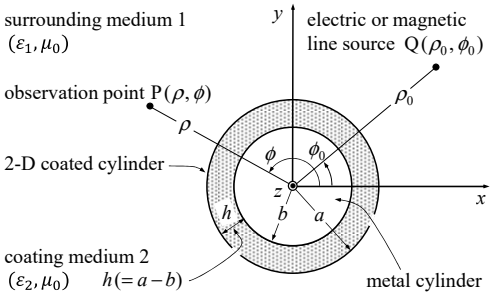

Fig. 1 Cross-sectional geometry of a 2-D coated cylinder of outer radius $\rho = a$, and coordinate systems (x, y, z) and (ρ, ϕ). $\mathrm{Q}(\rho_0, \phi_0)$: electric or magnetic line source, $\mathrm{P}(\rho, \phi)$: observation point. The thickness h of a coating medium 2 is assumed to be greater than or equal to the minimum thickness h_c $(h \geq h_c)$ that satisfies the applicable condition of the scatterer information estimation method (see (A·3) in Appendix A).

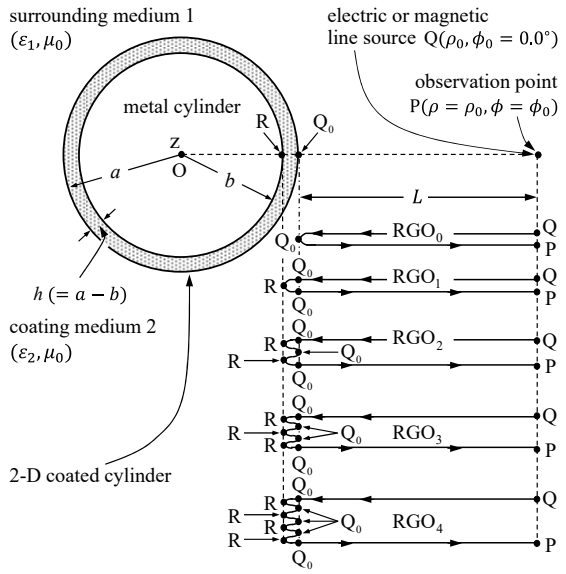

Fig. 2 Schematic diagram of backward transient scattering from a 2-D coated cylinder when a line source $Q(\rho_0, \phi_0 = 0.0^\circ)$ and an observation point $P(\rho, \phi)$ are at the same location. The propagation paths of backward transient scattering field components: $RGO_{p=0} = RGO_0(Q \rightarrow Q_0 \rightarrow P)$, $RGO_{p=1} = RGO_1(Q \rightarrow Q_0 \rightarrow R \rightarrow Q_0 \rightarrow P)$, and $RGO_p(Q \rightarrow p(Q_0 \rightarrow R \rightarrow) Q_0 \rightarrow P)$, $p = 2, 3, 4$. The propagation path $p\,(Q_0 \rightarrow R \rightarrow) Q_0$ represents multiple reflection effect in a coating medium 2. The p denotes the number of reflections at the point R on a metal surface of inner radius $\rho = b$.

series shown in (B·1) in Appendix B.

3. AIRs Using TD-SPT

3.1 UWB Pulse Source

It is assumed that the following truncated Gaussian-type modulated pulse source, $s(t)$, is located at the point Q [21]-[23], [25]-[29]:

$$s(t) = \begin{cases} \exp\left[-i\omega_0(t - t_0) - \dfrac{(t - t_0)^2}{(2d)^2}\right] & \text{for } 0 \le t \le 2t_0 \\ 0 & \text{elsewhere} \end{cases} \tag{1}$$

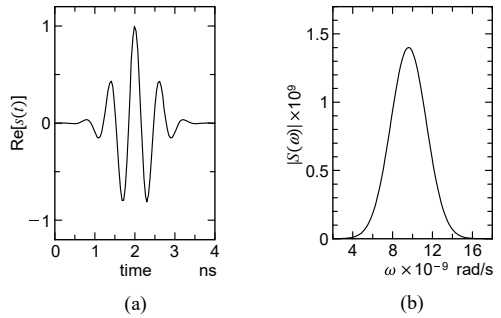

Fig. 3 Truncated Gaussian-type modulated UWB pulse source $s(t)$ defined by (1). (a) Real part of $s(t)$. (b) Absolute value of $S(\omega)$. Numerical parameters: $\omega_0 = 1.0 \times 10^{10}\,\mathrm{rad/s}$, $t_0 = 2.0 \times 10^{-9}\mathrm{s}$, and $d = 3.371 \times 10^{-10}\mathrm{s}$. The fractional bandwidth (FB) is 0.90, which satisfies the UWB definition (FB> 0.25) in [20].

where ω_0 is a central angular frequency, and t_0 and d are constant parameters. The frequency spectrum $S(\omega)$ of $s(t)$ is given by using the error function erf z [30].

$$S(\omega) = 2d\sqrt{\pi}\mathrm{Re}[\mathrm{erf}\beta(\omega)]\exp\{i\omega t_0 - d^2(\omega - \omega_0)^2\} \tag{2}$$

$$\beta(\omega) = \frac{t_0}{2d} - id(\omega - \omega_0) \tag{3}$$

$$\mathrm{erf}\, z = \frac{2}{\sqrt{\pi}}\int_0^z \exp(-t^2)\, dt. \tag{4}$$

Figures 3(a) and 3(b) show the real part of $s(t)$ in (1) and the absolute value of $S(\omega)$ in (2), respectively. With the numerical parameters depicted in Fig. 3, $s(t)$ in (1) represents the UWB pulse source (see Fig. 3 caption).

3.2 Derivation of AIRs using TD-SPT

The peak of the response waveform of each backward transient scattering field component in (B·2), which forms the TD-SPT in (B·1) shown in Appendix B, and its arrival time are given by [28]

$$\mathrm{Re}[y_{j,\,\mathrm{SPT},\,\mathrm{RGO}_p}(t_{\mathrm{RGO}_p})] = \mathrm{Re}[D(\omega_0)]A_{j,\mathrm{RGO}_p}\mathrm{erf}\beta(\omega_0), \quad p = 0, 1, \cdots, M_j \tag{5}$$

$$t = t_{\mathrm{RGO}_p} = t_0 + \frac{L_{\mathrm{RGO}_p}}{c_1}, p = 0, 1, \cdots, M_j. \tag{6}$$

In order to obtain (5) from (B·2), we employed the following relation:

$$\omega_{s,\mathrm{RGO}_p} = \omega_0 \ \text{ for } \ t = t_{\mathrm{RGO}_p}. \tag{7}$$

In the following section, we utilize the TD-SPT to derive the AIRs for both E- and H-polarizations [28]. It should be noted that the DGO component does not exist when a line source and an observation point are at the same location. Consequently, there is no $\mathrm{AIR}_{j,\mathrm{RGO}_0/\mathrm{DGO}}$, $j = \mathrm{E}, \mathrm{H}$ of the $\mathrm{RGO}_{p=0}(= \mathrm{RGO}_0)$ with respect to the DGO which is shown in (8) in [27].

First, we derive the $\mathrm{AIR}_{j,\mathrm{RGO}_1/\mathrm{RGO}_0}$, $j = \mathrm{E}, \mathrm{H}$ of $\mathrm{RGO}_{p=1}(= \mathrm{RGO}_1)$ with respect to $\mathrm{RGO}_{p=0}(= \mathrm{RGO}_0)$. To do so, we apply (B·6) and (B·12) to (5), which yields the $\mathrm{AIR}_{j,\mathrm{RGO}_1/\mathrm{RGO}_0}$ as follows:

$$\begin{aligned} \mathrm{AIR}_{j,\mathrm{RGO}_1/\mathrm{RGO}_0} &= \frac{\mathrm{Re}[y_{j,\,\mathrm{SPT},\,\mathrm{RGO}_1}(t_{\mathrm{RGO}_1})]}{\mathrm{Re}[y_{j,\,\mathrm{SPT},\,\mathrm{RGO}_0}(t_{\mathrm{RGO}_0})]} \\ &= \frac{\mathrm{Re}[D(\omega_0)]A_{j,\,\mathrm{RGO}_1}\mathrm{erf}\beta(\omega_0)}{\mathrm{Re}[D(\omega_0)]A_{j,\,\mathrm{RGO}_0}\mathrm{erf}\beta(\omega_0)} \\ &= \sqrt{\frac{2L(a + L)}{2L(a + L) + D_1}}(T_{j,12}T_{j,21})\left(\frac{R_{j,2}}{R_{j,11}}\right), \quad j = \mathrm{E}, \mathrm{H}. \end{aligned} \tag{8}$$

The $\mathrm{AIR}_{j,\mathrm{RGO}_1/\mathrm{RGO}_0}$ is expressed as the product of three influence factors: the divergence factor (square root term),

the transmission factor $(T_{j,12}T_{j,21})$ (see (B·16) and (B·17)), and the reflection factor $(R_{j,2}/R_{j,11})$ (see (B·11) and (B·18)).

Next, we derive the $\mathrm{AIR}_{j,\mathrm{RGO}_p/\mathrm{RGO}_{p-1}}$, $j = \mathrm{E}, \mathrm{H}, p = 2, 3, \cdots, M_j$ of RGO_p with respect to RGO_{p-1}. By applying (B·12) to (5), the $\mathrm{AIR}_{j,\mathrm{RGO}_p/\mathrm{RGO}_{p-1}}$ is given by

$$\mathrm{AIR}_{j,\mathrm{RGO}_p/\mathrm{RGO}_{p-1}} = \frac{\mathrm{Re}[y_{j,\,\mathrm{SPT},\,\mathrm{RGO}_p}(t_{\,\mathrm{RGO}_p})]}{\mathrm{Re}[y_{j,\,\mathrm{SPT},\,\mathrm{RGO}_{p-1}}(t_{\,\mathrm{RGO}_{p-1}})]}$$

$$= \frac{\mathrm{Re}[D(\omega_0)]A_{j,\,\mathrm{RGO}_p}\mathrm{erf}\beta(\omega_0)}{\mathrm{Re}[D(\omega_0)]A_{j,\,\mathrm{RGO}_{p-1}}\mathrm{erf}\beta(\omega_0)}$$

$$= \sqrt{\frac{2L(a+L)+D_{p-1}}{2L(a+L)+D_p}}\,(R_{j,2}R_{j,22}),$$

$$j = \mathrm{E}, \mathrm{H}, p = 2, 3, \cdots, M_j. \quad (9)$$

The $\mathrm{AIR}_{j,\mathrm{RGO}_p/\mathrm{RGO}_{p-1}}$ is expressed as the product of two influence factors: the divergence factor (square root term) and the reflection factor $(R_{j,2}R_{j,22})$ (see (B·18) and (B·19)).

3.3 Polarization independence of AIRs

Substituting (B·11) and from (B·16) to (B·18) into (8) gives

$$\mathrm{AIR}_{\mathrm{E},\mathrm{RGO}_1/\mathrm{RGO}_0} = \mathrm{AIR}_{\mathrm{H},\mathrm{RGO}_1/\mathrm{RGO}_0}$$

$$= \sqrt{\frac{2L(a+L)}{2L(a+L)+D_1}}\,\frac{4\sqrt{\varepsilon_{1r}\varepsilon_{2r}}}{\varepsilon_{2r}-\varepsilon_{1r}}. \quad (10)$$

Substitution of (B·18) and (B·19) into (9) yields

$$\mathrm{AIR}_{\mathrm{E},\mathrm{RGO}_p/\mathrm{RGO}_{p-1}} = \mathrm{AIR}_{\mathrm{H},\mathrm{RGO}_p/\mathrm{RGO}_{p-1}}$$

$$= \sqrt{\frac{2L(a+L)+D_{p-1}}{2L(a+L)+D_p}}\,\frac{\sqrt{\varepsilon_{1r}}-\sqrt{\varepsilon_{2r}}}{\sqrt{\varepsilon_{2r}}+\sqrt{\varepsilon_{1r}}},$$

$$p = 2, 3, \cdots, M_j. \quad (11)$$

By combining (10) with (11), the AIRs of the E-polarization and the H-polarization are expressed by the following relationship:

$$\mathrm{AIR}_{\mathrm{E},\mathrm{RGO}_p/\mathrm{RGO}_{p-1}} = \mathrm{AIR}_{\mathrm{H},\mathrm{RGO}_p/\mathrm{RGO}_{p-1}},$$

$$p = 1, 2, 3, \cdots, M_j. \quad (12)$$

Analytical confirmation can be provided from the relationship in (12) that both the AIRs in (8) and (9) are independent of polarization. The polarization independence of the AIRs in (12) will be verified numerically in Section 5.3.

4. Scatterer Information Estimation Method by TD-SPT

4.1 Simulation Model

In this section, we introduce a simulation model that will be utilized in the scatterer information estimation method to be proposed in Section 4.3. Since there is no DGO component when a line source and an observation point are at the same location, it is challenging to derive an estimation formula for the relative permittivity ε_{1r} of the surrounding medium 1 which is shown in (11) in [27]. The three types of scatterer information are the relative permittivity ε_{2r} of a coating medium 2 and its thickness h, and the outer radius a of a coated cylinder.

4.1.1 Assumptions for the Estimation Method and Notations

Initially, the scatterer information estimation method assumes the following:

(A) The structure of a scatterer is a 2-D coated cylinder covered with a uniform coating medium layer.

(B) The numerical parameters (ω_0, t_0, d) of a pulse source $s(t)$ in (1) are known.

(C) The pulse wave is radiated from a line source Q placed parallel to the central axis of a coated cylinder, and a line source Q and an observation point P are at the same location.

(D) The outer radius of a scatterer is sufficiently large compared to the wavelength of the central angular frequency ω_0 of a pulse source $s(t)$.

(E) At an observation point P, the peak of the response waveform of each backward transient scattering field component and its arrival time can be observed with high accuracy.

The estimation method then employs the following notations (Ȧ) and (Ḃ).

(Ȧ) Estimates are indicated by a caret "^" and denoted as $\hat{\varepsilon}_{2r}$, $\hat{h}$, and $\hat{a}$.

(Ḃ) Numerical data observed in the response waveforms, numerical parameters of a pulse source $s(t)$, and set values are marked with the overline symbol "‾" and denoted as $\overline{\mathrm{Re}[y_{j,\,\mathrm{SPT},\mathrm{RGO}_p}(\bar{t}_{\mathrm{RGO}_p})]}$, $\bar{t}_{\mathrm{RGO}_p}$, $\bar{t}_0$, and $\bar{\varepsilon}_{2r}$, etc.

4.1.2 Simulation Model and Numerical Data of Response Waveforms

Figure 4(a) shows a schematic diagram of a 2-D coated cylinder of outer radius $\hat{a}$ coated with a coating medium layer $(\varepsilon_0\hat{\varepsilon}_{2r}, \mu_0)$ of thickness $\hat{h}$. A line source Q and an

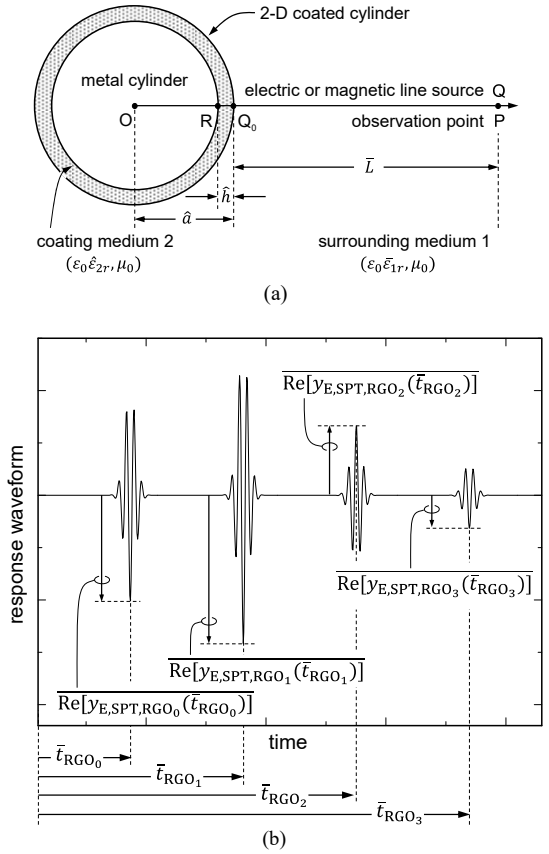

Fig. 4 Simulation model of a scatterer information estimation method. (a) Schematic diagram of a 2-D coated cylinder, an electric or magnetic line source Q and an observation point P are at the same location. Q_0 : a point on a coating surface of outer radius $\hat{a}$, R : a point on a metal surface of inner radius $\hat{a}-\hat{h}$. (b) An example of the response waveforms of backward transient scattering electric field components. Also shown are numerical data for four sets of peaks and their arrival times calculated from (5) and (6), respectively.

observation point P are placed at the same location in a surrounding medium 1 $(\varepsilon_0\bar{\varepsilon}_{1r},\mu_0)$.

Figure 4(b) shows an example of the response waveforms of the backward transient scattering electric field components. The numerical data of the peaks and their arrival times of $\mathrm{RGO}_p, p=0,1,2,3$ calculated from (5) and (6) are represented by $\overline{\mathrm{Re}[y_{\mathrm{E,\,SPT,RGO}_p}(\bar{t}_{\mathrm{RGO}_p})]}$ and $\bar{t}_{\mathrm{RGO}_p}$, respectively.

4.2 Derivation of Scatterer Information Estimation Formulas

In the absence of a DGO component when a line source and observation point are at the same location, there is no $\mathrm{AIR}_{j,\mathrm{RGO}_0/\mathrm{DGO}}$, $j=\mathrm{E},\mathrm{H}$. In this section, we derive the three types of estimation formulas $(\hat{\varepsilon}_{2r},\hat{h},\hat{a})$ of the scatterer information (ε_{2r},h,a) by applying the TD-SPT in Appendix B, the numerical data of the response waveforms of the backward transient scattering field components, and the numerical parameters of a pulse source $s(t)$ in (1) to the two types of AIRs derived in Section 3.2.

4.2.1 Estimation Formula $\hat{\varepsilon}_{2r}$ of the Relative Permittivity ε_{2r}

Substituting (B·8) into (6), we obtain the distance QQ_0 ($\mathrm{Q}_0\mathrm{P}$) from the source point Q (point Q_0) to the point Q_0 (observation point P)

$$\bar{L}=\frac{c_1}{2}(\bar{t}_{\mathrm{RGO}_0}-\bar{t}_0)=\mathrm{QQ}_0=\mathrm{Q}_0\mathrm{P} \tag{13}$$

where point Q_0 is the point on a coating surface of outer radius $\rho=a$ (see Fig. 4(a)). In deriving (13), t_{RGO_0} and t_0 are replaced by the numerical data $\bar{t}_{\mathrm{RGO}_0}$ and the numerical parameter $\bar{t}_0$, respectively. Thus, substituting $\bar{t}_{\mathrm{RGO}_0}$ and $\bar{t}_0$, as well as the speed of light c_1 in the surrounding medium 1 (see (B·4)) into (13), we obtain $\bar{L}$ numerically.

Substituting (B·18) and (B·19) into (9) yields the following formula:

$$\hat{\varepsilon}_{2r}=\left(\frac{\bar{\Lambda}_{p/p-1}-\bar{A}_{j,p/p-1}}{\bar{\Lambda}_{p/p-1}+\bar{A}_{j,p/p-1}}\right)^2\bar{\varepsilon}_{1r},\ p=2,3,\cdots,M_j \tag{14}$$

$$\bar{\Lambda}_{p/p-1}=\sqrt{\frac{2\bar{L}(\hat{a}+\bar{L})+\overline{D}_{p-1}}{2\bar{L}(\hat{a}+\bar{L})+\overline{D}_p}} \tag{15}$$

$$\overline{D}_p=p\frac{(\hat{a}+\bar{L})^2(2\hat{h})}{\hat{a}-\hat{h}}\sqrt{\frac{\bar{\varepsilon}_{1r}}{\hat{\varepsilon}_{2r}}} \tag{16}$$

$$\bar{A}_{j,p/p-1}=\overline{\mathrm{AIR}_{j,\mathrm{RGO}_p/\mathrm{RGO}_{p-1}}}=\frac{\overline{\mathrm{Re}[y_{j,\,\mathrm{SPT},\,\mathrm{RGO}_p}(\bar{t}_{\mathrm{RGO}_p})]}}{\overline{\mathrm{Re}[y_{j,\,\mathrm{SPT},\,\mathrm{RGO}_{p-1}}(\bar{t}_{\mathrm{RGO}_{p-1}})]}} \tag{17}$$

where $\bar{\Lambda}_{p/p-1}$ in (15) is a divergence factor. In the derivation of $\overline{D}_p$ in (16), a, h, and ε_{2r} as well as ε_{1r} and L are replaced by the estimates $\hat{a}$, $\hat{h}$, and $\hat{\varepsilon}_{2r}$, and the numerical data $\bar{\varepsilon}_{1r}$ and $\bar{L}$, respectively. $\bar{A}_{j,p/p-1}$ in (17) is the numerical data of $\mathrm{AIR}_{j,\mathrm{RGO}_p/\mathrm{RGO}_{p-1}}$ in (9) obtained from Fig. 4(b). Therefore, by substituting $\bar{\varepsilon}_{1r}$, $\bar{\Lambda}_{p/p-1}$, and $\bar{A}_{j,p/p-1}$ into (14), the estimate of $\hat{\varepsilon}_{2r}$ is obtained numerically.

While $\hat{\varepsilon}_{2r}$ in (14) can be simplified by approximating $\bar{\Lambda}_{p/p-1}$ in (15) with one as follows:

$$\hat{\varepsilon}_{2r}=\left(\frac{1-\bar{A}_{j,p/p-1}}{1+\bar{A}_{j,p/p-1}}\right)^2\bar{\varepsilon}_{1r},\ p=2,3,\cdots,M_j. \tag{18}$$

4.2.2 Estimation Formula $\hat{h}$ of the Thickness h

Substituting (B·4) and (B·15) into (6), we obtain

$$\hat{h} = \frac{c_0}{2\sqrt{\hat{\varepsilon}_{2r}}}\left(\overline{t}_{\mathrm{RGO}_p} - \overline{t}_{\mathrm{RGO}_{p-1}}\right), p = 1,2,\cdots,M_j. \quad (19)$$

In the derivation of $\hat{h}$ in (19), t_{RGO_p} and $t_{\mathrm{RGO}_{p-1}}$ are replaced by the numerical data $\overline{t}_{\mathrm{RGO}_p}$ and $\overline{t}_{\mathrm{RGO}_{p-1}}$, respectively. Consequently, by substituting the speed of light c_0 in free space (see (B·4)), $\overline{t}_{\mathrm{RGO}_p}$, $\overline{t}_{\mathrm{RGO}_{p-1}}$, and $\hat{\varepsilon}_{2r}$ into (19), we can obtain the estimate of $\hat{h}$ numerically.

4.2.3 Estimation Formula $\hat{a}$ of the Outer Radius a

Substituting (B · 16) to (B · 19) into (8), we obtain the following formula:

$$\hat{a} = \frac{2\bar{L}\hat{h}\left[(\bar{A}_{j,1/0})^2 - \hat{E}^2\right] - \bar{L}\hat{F}(\bar{A}_{j,1/0})^2}{2\bar{L}\left[(\bar{A}_{j,1/0})^2 - \hat{E}^2\right] + \hat{F}(\bar{A}_{j,1/0})^2} \quad (20)$$

$$\hat{E} = \frac{4\sqrt{\bar{\varepsilon}_{1r}\hat{\varepsilon}_{2r}}}{\hat{\varepsilon}_{2r} - \bar{\varepsilon}_{1r}} \quad (21)$$

$$\hat{F} = 2\hat{h}\sqrt{\frac{\bar{\varepsilon}_{1r}}{\hat{\varepsilon}_{2r}}} \quad (22)$$

$$\bar{A}_{j,1/0} = \overline{\mathrm{AIR}_{j,\mathrm{RGO}_1/\mathrm{RGO}_0}} = \frac{\overline{\mathrm{Re}[y_{j,\,\mathrm{SPT},\,\mathrm{RGO}_1}(\overline{t}_{\mathrm{RGO}_1})]}}{\overline{\mathrm{Re}[y_{j,\,\mathrm{SPT},\,\mathrm{RGO}_0}(\overline{t}_{\mathrm{RGO}_0})]}}. \quad (23)$$

The numerical data of $\mathrm{AIR}_{j,\mathrm{RGO}_1/\mathrm{RGO}_0}$ in (8), represented by $\bar{A}_{j,1/0}$ in (23), is obtained from Fig. 4(b). In deriving $\hat{a}$ in (20), the values of h and ε_{2r}, as well as ε_{1r} and L, are replaced by the estimates $\hat{h}$ and $\hat{\varepsilon}_{2r}$ and the numerical data $\bar{\varepsilon}_{1r}$ and $\bar{L}$, respectively. Consequently, by substituting $\bar{A}_{j,1/0}$, $\hat{h}$, $\hat{\varepsilon}_{2r}$, $\bar{\varepsilon}_{1r}$, and $\bar{L}$ into (20), we can obtain the estimate of $\hat{a}$ numerically.

4.3 Scatterer Information Estimation Method

In this section, we present a method to obtain the estimates $(\hat{\varepsilon}_{2r}, \hat{h}, \hat{a})$ of the scatterer information (ε_{2r}, h, a) by substituting the numerical data of the response waveforms of backward transient scattering field components presented in Section 4.1 and the numerical parameters of the pulse source $s(t)$ in (1) into the estimation formulas derived in Section 4.2 and performing the iterative calculations.

(a) First, set the number of reflections p used in the estimation formulas (see Section 4.2), the convergence degree ε, the initial value $I = 1$ of the number of iterations I, and its upper limit $I = I_{\mathrm{MAX}}$.

(b) Substituting the numerical data $\bar{A}_{j,p/p-1}$ and $\bar{\varepsilon}_{1r}$ into (18), a simplified estimate $\hat{\varepsilon}_{2r} = \hat{\varepsilon}_{2r,I}$ can be obtained. The subscript I indicates the number of iterations.

(c) Substituting the numerical data $\overline{t}_{\mathrm{RGO}_p}$, $\overline{t}_{\mathrm{RGO}_{p-1}}$, and the estimate $\hat{\varepsilon}_{2r,I}$ obtained in (b) into (19), we obtain the estimate $\hat{h} = \hat{h}_I$.

(d) Substituting the numerical data $\bar{\varepsilon}_{1r}$, $\bar{L}$, and $\bar{A}_{j,1/0}$ along with the estimates $\hat{h}_I$ and $\hat{\varepsilon}_{2r,I}$ into (20) yields the estimate $\hat{a} = \hat{a}_I$.

(e) Calculating $\overline{D}_p$ in (16) using $\bar{L}$, $\bar{\varepsilon}_{1r}$, $\hat{\varepsilon}_{2r}$, $\hat{h}$, and $\hat{a}$, followed by the updating of $\bar{\Lambda}_{p/p-1}$ in (15) using $\bar{L}$, $\hat{a}$, $\overline{D}_p$, and $\overline{D}_{p-1}$.

(f) Substituting the numerical data $\bar{\varepsilon}_{1r}$, $\bar{\Lambda}_{p/p-1}$, and $\bar{A}_{j,p/p-1}$ into (14) yields a new estimate $\hat{\varepsilon}_{2r} = \hat{\varepsilon}_{2r,I}$ with improved accuracy compared to (b).

(g) To count the number of iterations, the value of I is incremented by one. Then, new estimates $\hat{h} = \hat{h}_{I+1}$, $\hat{a} = \hat{a}_{I+1}$, and $\hat{\varepsilon}_{2r} = \hat{\varepsilon}_{2r,I+1}$ are obtained in (c), (d), and (f). Iterate the calculations in (c), (d), (e), and (f) to improve the accuracy of the estimates.

(h) Calculate the convergence values of the estimates using the following equation

$$|\Delta\hat{X}| < \varepsilon \quad (24)$$

$$\Delta\hat{X} = \frac{\hat{X}_I - \hat{X}_{I-1}}{\hat{X}_I} \text{ for } X = \varepsilon_{2r}, h, a. \quad (25)$$

In (24), convergence to the set value is considered to have occurred if the relative difference $|\Delta\hat{X}|$ between the previous estimate $\hat{X}_{I-1}$ and the new estimate $\hat{X}_I$ is less than the convergence degree ε. After storing I in I_{END}, proceed with (j).

(i) If I satisfies I_{MAX}, store I_{MAX} in I_{END} and then proceed with (j).

(j) Finally, output the estimates $(\hat{\varepsilon}_{2r}, \hat{h}, \hat{a})$ and the number of iterations I_{END}.

The estimation errors $\delta\hat{X}$, $X = \varepsilon_{2r}, h, a$ of the estimates $\hat{X}$ for the set values $\overline{X}$ are defined as follows:

$$\delta\hat{X} = \frac{\hat{X} - \overline{X}}{\overline{X}} \text{ for } X = \varepsilon_{2r}, h, a. \quad (26)$$

The degree of influence of the three factors that comprise the estimation error $\delta\hat{\varepsilon}_{2r}$ in the estimate $\hat{\varepsilon}_{2r}$ will be discussed in Sections 5.4 and 5.5. The aforementioned three factors are the convergence degree ε, the ratio $\Delta\hat{\varepsilon}_{2r}/\varepsilon$ of $\Delta\hat{\varepsilon}_{2r}$ in (25) to ε, and the ratio $\delta\hat{\varepsilon}_{2r}/\Delta\hat{\varepsilon}_{2r}$ of $\delta\hat{\varepsilon}_{2r}$ in (26) to $\Delta\hat{\varepsilon}_{2r}$.

4.4 Deriving Approximations for Estimation Errors

In this section, we derive the approximations $\delta\hat{X}_{\mathrm{asy}}, X = h, a$ for the estimation errors $\delta\hat{X}, X = h, a$ of the estimates $\hat{X}, X = h, a$ obtained in Section 4.3 using the estimation formulas in Section 4.2.

An approximation formula for the estimate $\hat{\varepsilon}_{2r}$ of the relative permittivity ε_{2r} is given by the following equation, in which the set value $\bar{\varepsilon}_{2r}$ and the estimation error $\delta\hat{\varepsilon}_{2r}$ in $\hat{\varepsilon}_{2r}$ are used.

$$\hat{\varepsilon}_{2r} = \bar{\varepsilon}_{2r}(1 + \delta\hat{\varepsilon}_{2r}) \text{ for } |\delta\hat{\varepsilon}_{2r}| \ll 1. \quad (27)$$

First, we derive the estimation error $\delta\hat{h}$ in the estimate $\hat{h}$ of the thickness h. Substituting (27) into (19), we obtain the following approximation formula for $\hat{h}$

$$\hat{h} = \bar{h}(1 + \delta\hat{h}) \sim \bar{h}(1 + \delta\hat{h}_{\text{asy}}) \quad (28)$$

$$\bar{h} = \frac{c_0}{2\sqrt{\bar{\varepsilon}_{2r}}}\left(\bar{t}_{\text{RGO}_p} - \bar{t}_{\text{RGO}_{p-1}}\right), p = 1,2,\cdots,M_j \quad (29)$$

where $\bar{h}$ is the set value and the approximation $\delta\hat{h}_{\text{asy}}$ of $\delta\hat{h}$ is given by

$$\delta\hat{h} \sim \delta\hat{h}_{\text{asy}} = -\delta\hat{\varepsilon}_{2r}/2. \quad (30)$$

In deriving (28), we employed the following first-order approximate expression

$$(1 + x)^n \sim 1 + nx \text{ for } |x| \ll 1. \quad (31)$$

Next, we derive the estimation error $\delta\hat{a}$ in the estimate $\hat{a}$ of the outer radius a. Substituting (27) and (28) into (20) associated with (21), (22) and (23) and then using the first-order approximate expression in (31) gives an approximation formula for $\hat{a}$.

$$\hat{a} = \bar{a}(1 + \delta\hat{a}) \sim \bar{a}(1 + \delta\hat{a}_{\text{asy}}) \quad (32)$$

where $\bar{a}$ is the set value and the approximation $\delta\hat{a}_{\text{asy}}$ of $\delta\hat{a}$ is given by

$$\delta\hat{a} \sim \delta\hat{a}_{\text{asy}} = -\frac{2\bar{L}\bar{E}^2 + \bar{F}(\bar{A}_{j,1/0})^2}{2\bar{L}\left[(\bar{A}_{j,1/0})^2 - \bar{E}^2\right] + \bar{F}(\bar{A}_{j,1/0})^2}\delta\hat{\varepsilon}_{2r} \quad (33)$$

$$\bar{E} = \frac{4\sqrt{\bar{\varepsilon}_{1r}\bar{\varepsilon}_{2r}}}{\bar{\varepsilon}_{2r} - \bar{\varepsilon}_{1r}} \quad (34)$$

$$\bar{F} = 2\bar{h}\sqrt{\frac{\bar{\varepsilon}_{1r}}{\bar{\varepsilon}_{2r}}}. \quad (35)$$

The approximations $\delta\hat{X}_{\text{asy}},\ X = h, a$ for the estimation errors $\delta\hat{X},\ X = h, a$ are given by (30) and (33) using the estimation error $\delta\hat{\varepsilon}_{2r}$. These approximations $\delta\hat{X}_{\text{asy}},\ X = h, a$ are useful for the analytical interpretation of the estimation error $\delta\hat{X}$ in the estimate $\hat{X}$ obtained by the estimation method in Section 4.3.

The effectiveness of the interpretation method for the estimation errors $\delta\hat{X},\ X = h, a$ using the approximations $\delta\hat{X}_{\text{asy}},\ X = h, a$ will be demonstrated in Sections 5.4, 5.5, and 5.6.

4.5 Polarization Independence of the Estimation Formulas

In this section, we analytically clarify the polarization independence of the three types of estimation formulas $(\hat{\varepsilon}_{2r}, \hat{h}, \hat{a})$ of the scatterer information derived in Section 4.2, by focusing on the analytical results that the AIRs are independent of polarization, as revealed in Section 3.3.

First, we consider the independence of the simplified formula $\hat{\varepsilon}_{2r}$ in (18) with respect to polarization. The $\hat{\varepsilon}_{2r}$ used as the initial value in the estimation method is obtained by substituting the numerical data $\bar{\varepsilon}_{1r}$ and $\bar{A}_{j,p/p-1}$ into (18). Since $\bar{A}_{j,p/p-1}$ in (17) is polarization independent, it can be analytically confirmed that $\hat{\varepsilon}_{2r}$ in (18) is polarization independent.

Next, we examine the polarization independence of $\hat{h}$ in (19). Since $\hat{\varepsilon}_{2r}$ in (18) is polarization independent, it is easy to verify that $\hat{h}$ in (19) is polarization independent.

Third, we consider the polarization independence of $\hat{a}$ in (20). The $\hat{a}$ is obtained by substituting $\bar{A}_{j,1/0}$, $\hat{h}$, $\hat{\varepsilon}_{2r}$, $\bar{\varepsilon}_{1r}$, and $\bar{L}$ into (20). Since $\bar{A}_{j,1/0}$ in (23) is independent of polarization, it can be analytically confirmed that $\hat{a}$ in (20) is independent of polarization.

Finally, we consider the polarization independence of the highly accurate $\hat{\varepsilon}_{2r}$ in (14). The $\hat{\varepsilon}_{2r}$ is obtained by substituting $\bar{\Lambda}_{p/p-1}$, $\bar{A}_{j,p/p-1}$, and $\bar{\varepsilon}_{1r}$ into (14). Since $\bar{\Lambda}_{p/p-1}$, $\bar{A}_{j,p/p-1}$, and $\bar{\varepsilon}_{1r}$ are independent of polarization, it is analytically confirmed that $\hat{\varepsilon}_{2r}$ in (14) is independent of polarization.

From the above discussions, it is analytically confirmed that the three types of estimation formulas $(\hat{\varepsilon}_{2r}, \hat{h}, \hat{a})$ of the scatterer information derived in Section 4.2 are polarization independent. The polarization independence of the estimation formulas is verified numerically in Section 5.3.

5. Numerical Results and Discussions

In this section, we first evaluate the calculation accuracy and effectiveness of TD-SPT and extract the numerical data of the response waveforms of the backward transient scattering field components needed for the estimation. Then, we clarify the effectiveness of the scatterer information estimation method and the polarization independence of the estimation formulas. We discuss the accuracy of the estimates using the approximations to the estimation errors. Furthermore, we discuss the discrepancies that arise between the estimation errors when a line source and an observation point are at different locations which is shown in [27] and those when a line source and an observation point are at the same location. Finally, we discuss the methods to control the estimation accuracy and the computation time.

In the following numerical calculations, the common factor $D(\omega_0)$ in (B·3), where ω is replaced by ω_0, is assumed to be unity $(D(\omega_0) = 1)$.

5.1 Calculation Accuracy and Effectiveness of TD-SPT

Figures 5(a) and 5(b) show the response waveforms of the backward transient scattering fields for E- and H-polarizations, respectively. The numerical parameters used in the calculations are given in the caption of Fig. 5. In this case, the numerical parameters in Fig. 5 satisfy the applicable condition $(t_2 \geq t_0)$ for the time in (A·1) and the applicable condition $(h \geq h_c)$ for the thickness of a coating medium layer in (A·3).

We evaluate the calculation accuracy and effectiveness of TD-SPT for E-polarization. In Fig. 5(a), $\mathrm{Re}[y_{\mathrm{E,\,TD\text{-}SPT}}(t)]$

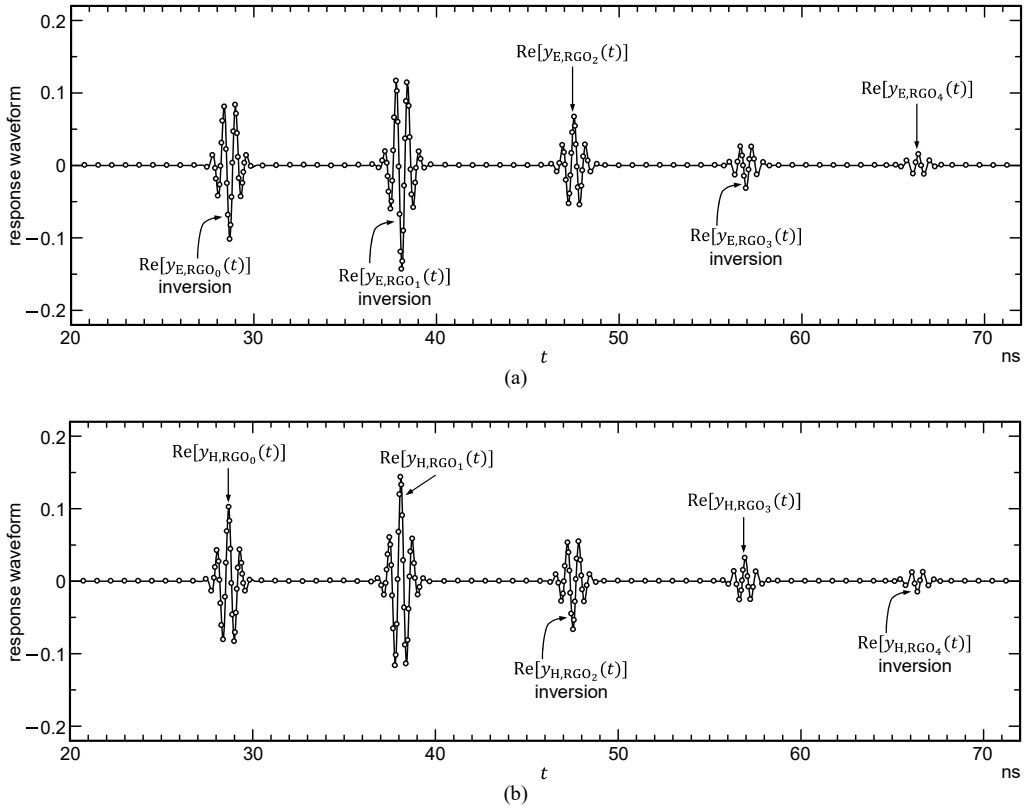

Fig. 5 Response waveforms of backward transient scattering fields for E- and H-polarizations under the condition $\varepsilon_1 < \varepsilon_2$. The numerical parameters used in the calculations are $a = 2.0\mathrm{m}$, $\varepsilon_1 = \varepsilon_0\varepsilon_{1r}$, $\varepsilon_{1r} = 1$, $\varepsilon_2 = \varepsilon_0\varepsilon_{2r}$, $\varepsilon_{2r} = 9$, $t_2 = 9.4248 \times 10^{-9}\mathrm{s} > t_0\ (= 2.0 \times 10^{-9}\mathrm{s})$ (see (A · 1)), and $h = 0.47091\mathrm{m}\ (= 0.23546a) > h_c\ \big(= 0.099931\mathrm{m}\ (= 0.049966a)\big)$ (see (A·3)), source point $\mathrm{Q}(\rho_0, \phi_0) = (3.0a, 0.0^\circ)$, and observation point $\mathrm{P}(\rho, \phi) = (3.0a, 0.0^\circ)$. The pulse source $s(t)$ used in the calculations is the UWB pulse source shown in Fig. 3. (a) ——: $\mathrm{Re}[y_{\mathrm{E,\,TD\text{-}SPT}}(t)]$, ooo: $\mathrm{Re}[y_{\mathrm{E,reference}}(t)]$. (b) ——: $\mathrm{Re}[y_{\mathrm{H,\,TD\text{-}SPT}}(t)]$, ooo: $\mathrm{Re}[y_{\mathrm{H,\,reference}}(t)]$.

Table 1 Numerical data for five sets of peaks and their arrival times of $\mathrm{RGO}_p, p = 0, 1, \cdots, M_j(= 4), j = \mathrm{E}, \mathrm{H}$ for both E- and H-polarizations calculated from (5) and (6). Also shown are the numerical data of the AIRs calculated from (8) and (9). The numerical parameters used in the simulation experiments are the same as those used in Fig. 5. Here, the thickness h is $0.47091\ \mathrm{m}\ (= 0.23546a)$.

field components	peaks	AIRs	arrival times
RGO_0	$\overline{\mathrm{Re}[y_{\mathrm{E,SPT,RGO}_0}(\bar{t}_{\mathrm{RGO}_0})]} = -1.02059290512295 \times 10^{-1}$ $\overline{\mathrm{Re}[y_{\mathrm{H,SPT,RGO}_0}(\bar{t}_{\mathrm{RGO}_0})]} = +1.02059290512295 \times 10^{-1}$	–	$\bar{t}_{\mathrm{RGO}_0} = 2.86851276164242 \times 10^{-8}$ s
RGO_1	$\overline{\mathrm{Re}[y_{\mathrm{E,SPT,RGO}_1}(\bar{t}_{\mathrm{RGO}_1})]} = -1.42509470389423 \times 10^{-1}$ $\overline{\mathrm{Re}[y_{\mathrm{H,SPT,RGO}_1}(\bar{t}_{\mathrm{RGO}_1})]} = +1.42509470389423 \times 10^{-1}$	$\overline{\mathrm{AIR}_{\mathrm{E,RGO}_1/\mathrm{RGO}_0}} = \overline{\mathrm{AIR}_{\mathrm{H,RGO}_1/\mathrm{RGO}_0}} = +1.39634000661856 \times 10^{0}$	$\bar{t}_{\mathrm{RGO}_1} = 3.81099055771936 \times 10^{-8}$ s
RGO_2	$\overline{\mathrm{Re}[y_{\mathrm{E,SPT,RGO}_2}(\bar{t}_{\mathrm{RGO}_2})]} = +6.69290905681081 \times 10^{-2}$ $\overline{\mathrm{Re}[y_{\mathrm{H,SPT,RGO}_2}(\bar{t}_{\mathrm{RGO}_2})]} = -6.69290905681081 \times 10^{-2}$	$\overline{\mathrm{AIR}_{\mathrm{E,RGO}_2/\mathrm{RGO}_1}} = \overline{\mathrm{AIR}_{\mathrm{H,RGO}_2/\mathrm{RGO}_1}} = -4.69646616363229 \times 10^{-1}$	$\bar{t}_{\mathrm{RGO}_2} = 4.75346835379629 \times 10^{-8}$ s
RGO_3	$\overline{\mathrm{Re}[y_{\mathrm{E,SPT,RGO}_3}(\bar{t}_{\mathrm{RGO}_3})]} = -3.16531415310060 \times 10^{-2}$ $\overline{\mathrm{Re}[y_{\mathrm{H,SPT,RGO}_3}(\bar{t}_{\mathrm{RGO}_3})]} = +3.16531415310060 \times 10^{-2}$	$\overline{\mathrm{AIR}_{\mathrm{E,RGO}_3/\mathrm{RGO}_2}} = \overline{\mathrm{AIR}_{\mathrm{H,RGO}_3/\mathrm{RGO}_2}} = -4.72935479360730 \times 10^{-1}$	$\bar{t}_{\mathrm{RGO}_3} = 5.69594614987323 \times 10^{-8}$ s
RGO_4	$\overline{\mathrm{Re}[y_{\mathrm{E,SPT,RGO}_4}(\bar{t}_{\mathrm{RGO}_4})]} = +1.50536291442834 \times 10^{-2}$ $\overline{\mathrm{Re}[y_{\mathrm{H,SPT,RGO}_4}(\bar{t}_{\mathrm{RGO}_4})]} = -1.50536291442834 \times 10^{-2}$	$\overline{\mathrm{AIR}_{\mathrm{E,RGO}_4/\mathrm{RGO}_3}} = \overline{\mathrm{AIR}_{\mathrm{H,RGO}_4/\mathrm{RGO}_3}} = -4.75580887588600 \times 10^{-1}$	$\bar{t}_{\mathrm{RGO}_4} = 6.63842394595017 \times 10^{-8}$ s
		–	

Table 2 Set values, estimates, and estimation errors of scatterer information for E- and H-polarizations. The numerical data of response waveforms in Table 1 are used for the estimations. The numerical parameters used in the simulation experiments are $p = 4, \varepsilon = 1.0 \times 10^{-10}$, and $I_{\mathrm{MAX}} = 200$. The number of iterations is $I_{\mathrm{END}} = 117$.

scatterer information	set values	estimates	estimation errors
$\varepsilon_{2\mathrm{r}}$	$\bar{\varepsilon}_{2r} = 9.00000000000000$	$\hat{\varepsilon}_{2r} = 8.99999999995670$	$\delta\hat{\varepsilon}_{2r} = -4.8106 \times 10^{-12}$
h	$\bar{h} = 4.70912891817118 \times 10^{-1}$ m	$\hat{h} = 4.70912891818252 \times 10^{-1}$ m	$\delta\hat{h} = 2.4071 \times 10^{-12}$
a	$\bar{a} = 2.00000000000000$ m	$\hat{a} = 1.99999999991892$ m	$\delta\hat{a} = -4.0539 \times 10^{-11}$

(——— : solid line) set to $M_{\mathrm{E}} = 4$ (see (B·1)) agrees very well with the reference solution $\mathrm{Re}[y_{\mathrm{E,\ reference}}(t)]$ ($\circ\circ\circ$) [21], [22] using TD-ANS over the whole region. This allows us to verify the computational accuracy of TD-SPT. The calculation times for $\mathrm{Re}[y_{\mathrm{E,\ TD\text{-}SPT}}(t)]$ and $\mathrm{Re}[y_{\mathrm{E,\ reference}}(t)]$ are 0.0252 s and 0.1629 s, respectively. The calculation speed ratio of TD-SPT to the reference solution is 6.464, confirming the effectiveness of TD-SPT.

The calculation accuracy and effectiveness of TD-SPT for H-polarization shown in Fig. 5(b) can be verified in the same way as for E-polarization described above.

5.2 Extraction of Numerical Data Required for Estimation

Table 1 shows the numerical data of the peaks of the response waveforms $\mathrm{Re}[y_{j,\ \mathrm{SPT},\ \mathrm{RGO}_p}(t)], j = \mathrm{E}, \mathrm{H}, p = 0, 1, \cdots, M_j\ (= 4)$ and their arrival times, which are required for the estimation of the scatterer information. Comparing the numerical data, the following relationship is observed between the peaks for the E- and H-polarizations.

$$\overline{\mathrm{Re}[y_{\mathrm{E,\ SPT,\ RGO}_p}(\bar{t}_{\mathrm{RGO}_p})]} = -\overline{\mathrm{Re}[y_{\mathrm{H,\ SPT,\ RGO}_p}(\bar{t}_{\mathrm{RGO}_p})]} \quad \text{for } p = 0, 1, \cdots, M_j(= 4). \tag{36}$$

The sign reversal phenomena of the peaks of the response waveforms due to the difference of polarization in (36) are also observed in the response waveforms in Fig. 5. The reason for the sign reversal of the peaks is that the following relationship holds for $A_{j,\mathrm{RGO}_p}, j = \mathrm{E}, \mathrm{H}, p = 0, 1, \cdots, M_j(= 4)$ in (5).

$$R_{\mathrm{E},\,11} = -R_{\mathrm{H},\,11} \ \text{ for } p = 0 \tag{37}$$

$$(R_{\mathrm{E},\,2})^p = -(R_{\mathrm{H},\,2})^p \ \text{ for } p = 2n+1, n = 0, 1 \tag{38}$$

$$(R_{\mathrm{E},\,22})^{p-1} = -(R_{\mathrm{H},\,22})^{p-1} \ \text{ for } p = 2n, n = 1, 2. \tag{39}$$

The $\mathrm{Re}[y_{j,\ \mathrm{reference}}(t)], j$=E, H by TD-ANS using the Fast Fourier Transform (FFT) numerical code [31] can be calculated for each backward transient scattering field component. However, it is difficult for $\mathrm{Re}[y_{j,\ \mathrm{reference}}(t)]$ to derive the peaks of the backward transient scattering field components and their arrival times as analytical solutions. In contrast, TD-SPT can derive analytical solutions for the peaks of the backward transient scattering field components and their arrival times using (5) and (6), respectively. TD-SPT can also analytically interpret the sign reversal phenomena of the peaks of the response waveforms due to the difference of polarization using (5) associated with (B·6) and (B·12). From these excellent features of TD-SPT, we can confirm the practicality of TD-SPT.

5.3 Effectiveness of the Estimation Method and Polarization Independence of the Estimation Formulas

In this section, we verify the effectiveness of the estimation method proposed in Section 4.3 and the polarization independence of the estimation formulas clarified in Section 4.5. In the simulation experiments, the numerical data of the response waveforms of the backward transient scattering field components shown in Table 1 are used. The number of reflections p in the estimation formulas $\hat{\varepsilon}_{2r}$ in (14) and $\hat{h}$ in (19), the convergence degree ε of the estimates, and the upper limit I_{MAX} of the number of iterations are set to $p = 4$, $\varepsilon = 1.0 \times 10^{-10}$, and $I_{\mathrm{MAX}} = 200$, respectively.

First, we examine the effectiveness of the estimation method for E-polarization. Table 2 shows the set values $(\bar{\varepsilon}_{2r}, \bar{h}, \bar{a})$, estimates $(\hat{\varepsilon}_{2r}, \hat{h}, \hat{a})$, and estimation errors $(\delta\hat{\varepsilon}_{2r}, \delta\hat{h}, \delta\hat{a})$ of the scatterer information. Since the number of iterations I_{END} is 117 $(I_{\mathrm{END}} < I_{\mathrm{MAX}})$, the estimates $(\hat{\varepsilon}_{2r}, \hat{h}, \hat{a})$ satisfy the convergence condition in (24). From the high accuracy of the estimates $(\hat{\varepsilon}_{2r}, \hat{h}, \hat{a})$ shown in Table 2, we can verify the effectiveness of the estimation method for E-polarization.

Table 1 also shows the numerical data of the AIRs calculated from (8) and (9). From Table 1, we can observe the following relationship between the E-polarized AIRs and the H-polarized AIRs.

$$\overline{\mathrm{AIR}_{\mathrm{E,RGO}_p/\mathrm{RGO}_{p-1}}} = \overline{\mathrm{AIR}_{\mathrm{H,RGO}_p/\mathrm{RGO}_{p-1}}}, \quad p = 1, 2, 3,\ M_j(= 4). \tag{40}$$

From the relationship in (40), we can numerically verify the polarization independence of the AIRs in (12).

Second, we examine the effectiveness of the estimation method for H-polarization. The estimates $(\hat{\varepsilon}_{2r}, \hat{h}, \hat{a})$ for H-polarization were the same as in Table 2. Thus, the effectiveness of the estimation method for H-polarization can be verified in the same way as for E-polarization described above.

The fact that the estimates $(\hat{\varepsilon}_{2r}, \hat{h}, \hat{a})$ shown in Table 2 are identical for both E- and H-polarizations allow us to numerically verify the polarization independence of the estimation formulas, which was clarified analytically in

Section 4.5.

Finally, if the numerical parameters (ω_0, t_0, d) satisfy the applicable condition $(t_2 \geq t_0)$ shown in (A·1) for a pulse source $s(t)$ in (1), then the estimates $(\hat{\varepsilon}_{2r}, \hat{h}, \hat{a})$ can be computed using the estimation methods in Section 4.3. For example, the numerical parameters (ω_0, t_0, d) shown in Fig. 3 of [27] satisfy the applicable condition $(t_2 \geq t_0)$. Consequently, utilizing a pulse source $s(t)$ shown in Fig. 3 of [27], we obtain the same number of iterations I_{END}, estimates $(\hat{\varepsilon}_{2r}, \hat{h}, \hat{a})$, and estimation errors $(\delta\hat{\varepsilon}_{2r}, \delta\hat{h}, \delta\hat{a})$ as in Table 2 in this paper.

5.4 Discussion of the Accuracy of the Estimates

In this section, we examine the accuracy of the estimates $(\hat{\varepsilon}_{2r}, \hat{h}, \hat{a})$ using the approximations $\delta\hat{X}_{\mathrm{asy}}$, $X = h, a$ of the estimation errors $\delta\hat{X}$, $X = h, a$ derived in Section 4.4.

First, we will express the numerically obtained estimation error $\delta\hat{\varepsilon}_{2r}$ in (26) as the product of the factors affecting $\delta\hat{\varepsilon}_{2r}$. Fig. 6 shows the magnitudes of the estimation errors $|\delta\hat{\varepsilon}_{2r}|$ in (26) (———: solid line) and those of the convergences $|\Delta\hat{\varepsilon}_{2r}|$ in (25) (- - - - -: broken line) as the number of iterations I is varied. The numerical parameters utilized in the simulation experiments are the same as those used in Table 2. It should be noted that the differences between $|\delta\hat{\varepsilon}_{2r}|$ and $|\Delta\hat{\varepsilon}_{2r}|$ are not dependent on the number of iterations I and remain constant.

The numerical results for the ratio $\Delta\hat{\varepsilon}_{2r}/\varepsilon$ $(= \alpha_{\hat{\varepsilon}_{2r}})$ of the convergence value $\Delta\hat{\varepsilon}_{2r}$ in (25) to the convergence degree ε and the ratio $\delta\hat{\varepsilon}_{2r}/\Delta\hat{\varepsilon}_{2r}$ $(= \beta_{\hat{\varepsilon}_{2r}})$ of the error $\delta\hat{\varepsilon}_{2r}$ in (26) to $\Delta\hat{\varepsilon}_{2r}$ at the number of iterations $I_{\mathrm{END}} = 117$ are presented below.

$$\alpha_{\hat{\varepsilon}_{2r}} = \frac{\Delta\hat{\varepsilon}_{2r}}{\varepsilon} = \frac{-1.0719 \times 10^{-11}}{1.0 \times 10^{-10}} = -1.0719 \times 10^{-1} \sim -10^{-0.96985} \quad \text{for Table 2} \quad (41)$$

$$\beta_{\hat{\varepsilon}_{2r}} = \frac{\delta\hat{\varepsilon}_{2r}}{\Delta\hat{\varepsilon}_{2r}} = \frac{-4.8106 \times 10^{-12}}{-1.0719 \times 10^{-11}} = 4.4879 \times 10^{-1} \sim 10^{-0.34796} \quad \text{for Table 2.} \quad (42)$$

From (41) and (42), the estimation error $\delta\hat{\varepsilon}_{2r}$ can be expressed as the product of three factors ε $(= 1.0 \times 10^{-10})$, $\alpha_{\hat{\varepsilon}_{2r}}$, and $\beta_{\hat{\varepsilon}_{2r}}$.

$$\delta\hat{\varepsilon}_{2r} = \varepsilon\alpha_{\hat{\varepsilon}_{2r}}\beta_{\hat{\varepsilon}_{2r}} = -4.8106 \times 10^{-12} \sim -10^{-11.31780} \quad \text{for Table 2.} \quad (43)$$

Next, the accuracy of the estimates $\hat{X}$, $X = h, a$ will be evaluated quantitatively using the approximations $\delta\hat{X}_{\mathrm{asy}}$, $X = h, a$ derived in Section 4.4. Substituting the numerical parameters presented in the caption of Fig. 5, the numerical data for AIRs in Table 1, and the numerical value for $\delta\hat{\varepsilon}_{2r}$ in Table 2 or (43) into the approximations $\delta\hat{X}_{\mathrm{asy}}$, $X = h, a$ in (30) and (33), the following approximate results are

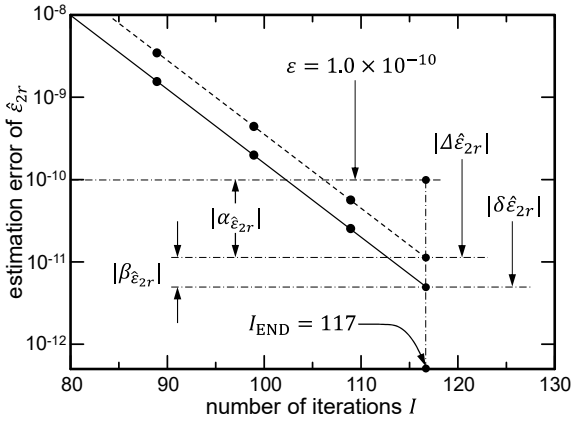

Fig. 6 The magnitudes of the estimation errors $|\delta\hat{\varepsilon}_{2r}|$ in (26) and those of the convergences $|\Delta\hat{\varepsilon}_{2r}|$ in (25) for E- and H-polarizations when the number of iterations I is varied under the condition that the number of reflections p of the estimation formulas $\hat{\varepsilon}_{2r}$ in (14) and $\hat{h}$ in (19) is fixed at $p = 4$. The numerical parameters utilized in the simulation experiments are the same as those used in Table 2, and $I_{\mathrm{END}} = 117$. ——●——: $|\delta\hat{\varepsilon}_{2r}|$, - -●- - : $|\Delta\hat{\varepsilon}_{2r}|$.

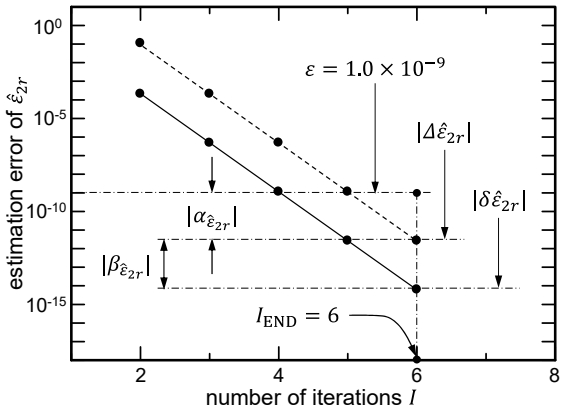

Fig. 7 The magnitudes of the estimation errors $|\delta\hat{\varepsilon}_{2r}|$ in (26) and those of the convergences $|\Delta\hat{\varepsilon}_{2r}|$ in (25) for E- and H-polarizations when the number of iterations I is varied. The numerical parameters utilized in the simulation experiments are the same as those used in Table 2 in [27], and $I_{\mathrm{END}} = 6$. ——●——: $|\delta\hat{\varepsilon}_{2r}|$, - -●- - : $|\Delta\hat{\varepsilon}_{2r}|$.

obtained

$$\delta\hat{h} \sim \delta\hat{h}_{\mathrm{asy}} = -0.5\delta\hat{\varepsilon}_{2r} = 2.4053 \times 10^{-12} \quad (44)$$

$$\delta\hat{a} \sim \delta\hat{a}_{\mathrm{asy}} = 10.399\delta\hat{\varepsilon}_{2r} = -5.0025 \times 10^{-11}. \quad (45)$$

As demonstrated in (46) and (47), the numerical confirmation can be provided that the approximations $\delta\hat{X}_{\mathrm{asy}}$, $X = h, a$ have good approximation accuracies to the estimation errors $\delta\hat{X}$, $X = h, a$ in Table 2.

$$|\delta\hat{h}_{\mathrm{asy}}/\delta\hat{h}| = 0.9993 \quad (46)$$

$$|\,\delta\hat{a}_{\mathrm{asy}}/\delta\hat{a}\,| = 1.2340. \quad (47)$$

From the approximate results in (44) and (45), it can be seen that $\hat{h}$ is twice as accurate as $\hat{\varepsilon}_{2r}$ (see (55)), while $\hat{a}$ is

approximately one order of magnitude less accurate than $\hat{\varepsilon}_{2r}$ (see (56)).

5.5 Comparison of Errors with Estimates in [27]

In this section, we calculate the estimation errors $(\delta\hat{\varepsilon}_{2r}, \delta\hat{h}, \delta\hat{a})$ of the estimates $(\hat{\varepsilon}_{2r}, \hat{h}, \hat{a})$ when a line source and an observation point are at different locations, as shown in [27], and discuss the discrepancies that arise between the estimation errors of the estimates when a line source and an observation point are at the same location as proposed in this paper.

Figure 7 shows the magnitudes of the estimation errors $|\delta\hat{\varepsilon}_{2r}|$ in (26) (———: solid line) and those of the convergences $|\Delta\hat{\varepsilon}_{2r}|$ in (25) (- - - - -: broken line) as the number of iterations I is varied. The numerical parameters utilized in the numerical experiments are the same as those used in Table 2 of [27]. It can be observed that the differences between $|\delta\hat{\varepsilon}_{2r}|$ and $|\Delta\hat{\varepsilon}_{2r}|$ are independent of the number of iterations I and remain constant.

The numerical results for $\alpha_{\hat{\varepsilon}_{2r}}$ in (41) and $\beta_{\hat{\varepsilon}_{2r}}$ in (42) at the number of iterations $I_{\mathrm{END}} = 6$ are presented below.

$$\alpha_{\hat{\varepsilon}_{2r}} = \frac{\Delta\hat{\varepsilon}_{2r}}{\varepsilon} = \frac{2.6758 \times 10^{-12}}{1.0 \times 10^{-9}} = 2.6758 \times 10^{-3} \sim 10^{-2.57255} \quad \text{for Table 2 in [27]} \tag{48}$$

$$\beta_{\hat{\varepsilon}_{2r}} = \frac{\delta\hat{\varepsilon}_{2r}}{\Delta\hat{\varepsilon}_{2r}} = \frac{6.3159 \times 10^{-15}}{2.6758 \times 10^{-12}} = 2.36038 \times 10^{-3} \sim 10^{-2.62702} \quad \text{for Table 2 in [27].} \tag{49}$$

Substituting the convergence degree $\varepsilon = 1.0 \times 10^{-9}$, (48), and (49) into (43) gives the following value for $\delta\hat{\varepsilon}_{2r}$:

$$\delta\hat{\varepsilon}_{2r} = \varepsilon\alpha_{\hat{\varepsilon}_{2r}}\beta_{\hat{\varepsilon}_{2r}} = 6.3159 \times 10^{-15} \sim 10^{-14.19956} \quad \text{for Table 2 in [27].} \tag{50}$$

The approximation formulas for the estimates $\hat{X},\ X = h, a$ were derived in the same way as in Section 4.4. Substituting numerical values into the approximation formulas yields the following approximate results for the errors $\delta\hat{X},\ X = h, a$:

$$\delta\hat{h} \sim \delta\hat{h}_{\mathrm{asy}} = -0.5\delta\hat{\varepsilon}_{2r} = -3.1580 \times 10^{-15} \quad \text{for Table 2 in [27]} \tag{51}$$

$$\delta\hat{a} \sim \delta\hat{a}_{\mathrm{asy}} = -1.018\delta\hat{\varepsilon}_{2r} = -6.4296 \times 10^{-15} \quad \text{for Table 2 in [27].} \tag{52}$$

As demonstrated in (53) and (54), we can confirm that the approximations $\delta\hat{X}_{\mathrm{asy}},\ X = h, a$ have good approximation accuracies to the estimation errors $\delta\hat{X},\ X = h, a$ in Table 2 of [27].

$$|\delta\hat{h}_{\mathrm{asy}}/\delta\hat{h}| = 1.1648 \tag{53}$$

$$|\delta\hat{a}_{\mathrm{asy}}/\delta\hat{a}| = 0.8644\,. \tag{54}$$

From the approximate results in (51) and (52), we can confirm that $\hat{h}$ in Table 2 of [27] is twice as accurate as $\delta\hat{\varepsilon}_{2r}$, while $\hat{a}$ is approximately as accurate as $\delta\hat{\varepsilon}_{2r}$.

A comparison of (43) and (50) reveals that the $\hat{\varepsilon}_{2r}$ proposed in this paper is less accurate than the $\hat{\varepsilon}_{2r}$ in [27] by $10^{2.88176} (= |-10^{-11.31780}/10^{-14.19956}|)$. The factor-by-factor impact of the accuracy degradation of $10^{2.88176}$ is 10^{-1} $(= 1.0 \times 10^{-10}/1.0 \times 10^{-9})$ for ε (see Table 2 in this paper and Table 2 in [27]), $10^{1.60270} (= |-10^{-0.96985}/10^{-2.57255}|)$ for $|\alpha_{\hat{\varepsilon}_{2r}}|$ (see (41) and (48)), and $10^{2.27906} (= |10^{-0.34796}/10^{-2.62702}|)$ for $|\beta_{\hat{\varepsilon}_{2r}}|$ (see (42) and (49)).

The discrepancy between the estimation error $\delta\hat{h}$ $(\delta\hat{a})$ in Table 2 of this paper and the estimation error $\delta\hat{h}$ $(\delta\hat{a})$ in Table 2 of [27] can be evaluated by comparing the approximate results of (44) and (51) ((45) and (52)).

5.6 Methods to Control Estimation Accuracy and Computation Time

The initial step in this section is to discuss a method for controlling the estimation accuracy of the estimates. Fig. 8 shows the magnitudes of the estimation errors $(\delta\hat{\varepsilon}_{2r}, \delta\hat{h}, \delta\hat{a})$ of the estimates $(\hat{\varepsilon}_{2r}, \hat{h}, \hat{a})$ and the number of iterations I_{END} for E-polarization when the convergence degree ε is varied under the condition that the value of the number of reflections p in the estimation formulas $\hat{\varepsilon}_{2r}$ in (14) and $\hat{h}$ in (19) is fixed at $p = 4$. It can be observed that for smaller (larger) values of ε, the estimation errors $(\delta\hat{\varepsilon}_{2r}, \delta\hat{h}, \delta\hat{a})$ become smaller (larger), while I_{END} becomes larger (smaller). Upon reduction of the value of ε by one order of magnitude, the estimation errors $(\delta\hat{\varepsilon}_{2r}, \delta\hat{h}, \delta\hat{a})$ become approximately one order of magnitude smaller (see three broken auxiliary lines (- - - - -) in Fig. 8), while the value of I_{END} increases by approximately 10 (see single dash-dotted auxiliary line (—·—·—) in Fig. 8). From the preceding discussions, it can be demonstrated that the estimation accuracy of the estimates for E-polarization can be controlled by varying ε with the value of p fixed.

From Fig. 8, it can be observed that the differences between the three types of estimation errors $(\delta\hat{\varepsilon}_{2r}, \delta\hat{h}, \delta\hat{a})$ are independent of ε and remain constant throughout the entire range of $10^{-11} \le \varepsilon \le 10^{-1}$. The ratios of the errors $\delta\hat{X}, X = h, a$ to the error $\delta\hat{\varepsilon}_{2r}$, utilizing the approximate results $\delta\hat{X}_{\mathrm{asy}}, X = h, a$ in (44) and (45), yield the following numerical results.

$$\left|\frac{\delta\hat{h}}{\delta\hat{\varepsilon}_{2r}}\right| \sim \left|\frac{\delta\hat{h}_{\mathrm{asy}}}{\delta\hat{\varepsilon}_{2r}}\right| = 0.5 \sim 10^{-0.301} \tag{55}$$

$$\left|\frac{\delta\hat{a}}{\delta\hat{\varepsilon}_{2r}}\right| \sim \left|\frac{\delta\hat{a}_{\mathrm{asy}}}{\delta\hat{\varepsilon}_{2r}}\right| = 10.399 \sim 10^{1.017}. \tag{56}$$

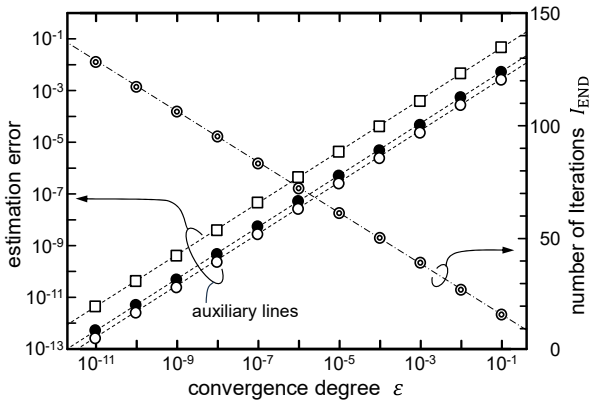

Fig. 8 The magnitudes of the estimation errors $(\delta\hat{\varepsilon}_{2r}, \delta\hat{h}, \delta\hat{a})$ and the number of iterations I_{END} for E- and H-polarizations are presented as a function of the convergence degree ε when the number of reflections p in the estimation formulas $\hat{\varepsilon}_{2r}$ in (14) and $\hat{h}$ in (19) is fixed at $p = 4$. The numerical parameters used in the simulation experiments are the same as those used in Fig. 5. ●●●: $|\delta\hat{\varepsilon}_{2r}|$, ○○○: $|\delta\hat{h}|$, □□□: $|\delta\hat{a}|$, ◎◎◎: number of iterations I_{END}.

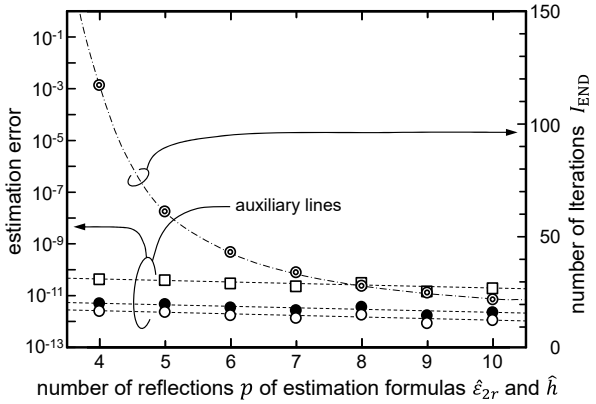

Fig. 9 The magnitudes of the estimation errors $(\delta\hat{\varepsilon}_{2r}, \delta\hat{h}, \delta\hat{a})$ and the number of iterations I_{END} for E- and H-polarizations are presented as a function of the number of reflections p in the estimation formulas $\hat{\varepsilon}_{2r}$ in (14) and $\hat{h}$ in (19) when the convergence degree ε is fixed at $\varepsilon = 1.0 \times 10^{-10}$. The numerical parameters used in the simulation experiments are the same as those used in Fig. 5. ●●●: $|\delta\hat{\varepsilon}_{2r}|$, ○○○: $|\delta\hat{h}|$, □□□: $|\delta\hat{a}|$, ◎◎◎: number of iterations I_{END}.

From (55), it can be observed that the estimate formula $\hat{h}$ in (19) provides an estimate that is twice as accurate as compared to $\hat{\varepsilon}_{2r}$. In contrast, from (56), we can confirm that the estimate formula $\hat{a}$ in (20) gives an estimate that is approximately one order of magnitude less accurate than that of $\hat{\varepsilon}_{2r}$.

While, the control of the estimation accuracy of the estimates for H-polarization when the value of ε is varied, under the condition that the value of p is fixed at $p = 4$, can be discussed in the same way as in the E-polarization case described above. Since the estimation formulas derived in Section 4.2 are polarization independent, the estimation errors and number of iterations for H-polarization were identical to those in Fig. 8. Consequently, a quantitative discussion of the method to control the estimation accuracy for H-polarization is also possible.

Secondly, we will discuss how to control the computation time of the estimation method. Fig. 9 shows the magnitudes of the estimation errors $(\delta\hat{\varepsilon}_{2r}, \delta\hat{h}, \delta\hat{a})$ of the estimates $(\hat{\varepsilon}_{2r}, \hat{h}, \hat{a})$ and the number of iterations I_{END} for E-polarization when the number of reflections p in the estimation formulas $\hat{\varepsilon}_{2r}$ in (14) and $\hat{h}$ in (19) is varied under the condition that the value of the convergence degree ε is fixed at $\varepsilon = 1.0 \times 10^{-10}$. No significant variations in the magnitudes of the estimation errors $(\delta\hat{\varepsilon}_{2r}, \delta\hat{h}, \delta\hat{a})$ are observed for the three types of estimates when the value of p is varied (see three broken auxiliary lines (- - - - -) in Fig. 9). Conversely, we observe a decrease (increase) in the value of I_{END} when the value of p is increased (decreased) (see single dash-dotted auxiliary line (−·−·−) in Fig. 9). This reduction (increase) in I_{END} indicates a reduction (increase) in the computation time required for the estimation method. Based on the preceding discussions, it can be confirmed that by varying p while the value of ε is fixed, the computation time of the estimation method can be controlled while ensuring the estimation accuracy of the estimates for E-polarization.

From Fig. 9, it can be observed that the differences between the three types of estimation errors $(\delta\hat{\varepsilon}_{2r}, \delta\hat{h}, \delta\hat{a})$ are independent of p and remain constant throughout the entire range of $4 \le p \le 10$. The ratios of the errors $\delta\hat{X}, X = h, a$ to the error $\delta\hat{\varepsilon}_{2r}$ are given by (55) and (56). Consequently, the quantitative evaluations of the errors $(\delta\hat{\varepsilon}_{2r}, \delta\hat{h}, \delta\hat{a})$ can be discussed in the same manner as in Fig. 8.

Similarly, controlling the computation time of the estimation method for H-polarization by varying p while the value of ε is fixed can be discussed in the same way as in the E-polarization case described above. As the estimation formulas derived in Section 4.2 are polarization independent, the estimation errors and the number of iterations for H-polarization were identical to those in Fig. 9. Consequently, it is also possible to discuss the quantitative aspects of controlling the computation time of the estimation method for H polarization.

6. Conclusions

This paper has presented a scatterer information estimation method for both E- and H-polarizations by TD-SPT utilizing numerical data of the response waveforms of the RGO series, which constitute the backward transient scattering field components when a line source and an observation point are at the same location. A 2-D coated cylinder was selected as the scatterer, and the thickness of a coating medium layer was assumed to satisfy the applicable condition of the estimation method.

Specifically, by applying the TD-SPT represented in

RGO series to AIRs, we have derived the three types of estimation formulas: the relative permittivity of a coating medium layer and its thickness, as well as the outer radius of a coated cylinder. By focusing on the polarization independence of AIRs, it was analytically demonstrated that all the estimation formulas for scatterer information denote the polarization independence. The estimates were obtained by substituting the numerical data of the response waveforms of the RGO components and the numerical parameters of a pulse source into the estimation formulas and performing iterative calculations. We derived approximations to the estimation errors that are useful in quantitatively evaluating the accuracy of the estimates obtained by the estimation method.

The effectiveness of the proposed estimation method was substantiated by a comparison of the estimates with the set values. The polarization independence of the estimation formulas was validated through a numerical comparison of the estimates for E- and H-polarizations. The estimation errors were discussed using the approximations to the errors of the estimates when a line source and an observation point were at the same location. The discrepancies that arise between the estimation errors when a line source and an observation point are at different locations were then discussed. Finally, the methods to control the estimation accuracy and computational time were also discussed.

References

[1] R.C. Hansen, ed., Geometric Theory of Diffraction, Part II, IEEE Press, New York, 1981.

[2] G.L. James, ed., Geometrical Theory of Diffraction for Electromagnetic Waves, chap.3, 3rd ed., Peter Peregrinus, London, 1986. DOI: 10.1049/pbew001e

[3] L.B. Felsen and N. Marcuvitz, eds., Radiation and Scattering of Waves, chap.6, IEEE Press, New York, 1994. DOI: 10.1109/9780470546307

[4] T.B.A. Senior and J.L. Volakis, eds., Approximate Boundary Conditions in Electromagnetics, chaps.3 and 7, IEE, London, 1995. DOI: 10.1049/pbew041e

[5] J.B. Keller, "Diffraction by a convex cylinder," I. R. E. Trans. on Antennas and Propagat., vol.AP-4, pp.312-321, Jul. 1956. DOI: 10.1109/tap.1956.1144427

[6] P.H. Pathak, "An asymptotic analysis of the scattering of plane waves by a smooth convex cylinder," Radio Science, vol.14, no.3, pp.419-435, May-Jun. 1979.

[7] P.H. Pathak, W.D. Burnside, and R.J. Marhefka, "A uniform GTD analysis of the diffraction of electromagnetic waves by a smooth convex surface," IEEE Trans. Antennas Propagat., vol.AP-28, no.5, pp.631-642, Sept. 1980. DOI: 10.1109/tap.1980.1142396

[8] N. Wang, "Electromagnetic scattering from a dielectric-coated circular cylinder," IEEE Trans. Antennas Propagat., vol.AP-33, no.9, pp.960-963, Sept. 1985. DOI: 10.1109/TAP.1985.1143696

[9] H.-T. Kim and N. Wang, "UTD solution for electromagnetic scattering by a circular cylinder with thin lossy coatings," IEEE Trans. Antennas Propagat., vol.37, no.11, pp.1463-1472, Nov. 1989. DOI: 10.1109/8.43566

[10] P. Hussar and R. Albus, "On the asymptotic frequency behavior of uniform GTD in the shadow region of a smooth convex surface," IEEE Trans. Antennas Propagat., vol.39, no.12, pp.1672-1680, Dec. 1991.

[11] P.E. Hussar, "A uniform GTD treatment of surface diffraction by impedance and coated cylinders," IEEE Trans. Antennas Propagat., vol.46, no.7, pp.998-1008, Jul. 1998. DOI: 10.1109/8.704801

[12] H. Vollmer and E.J. Rothwell, "Resonance series representation of the early-time field scattered by a coated cylinder," IEEE Trans. Antennas Propagat., vol.52, no.8, pp.2186-2190, Aug. 2004. DOI: 10.1109/TAP.2004.832331

[13] T. Ida and T. Ishihara, "Novel high-frequency asymptotic solutions in the transition regions near geometrical boundaries and near caustics for scattering by a dielectric cylinder," IEICE Trans. Electron., vol.E87-C, no.9, pp.1550-1559, Sept. 2004.

[14] T. Ida and T. Ishihara, "Novel high-frequency uniform asymptotic solution for scattered field by a conducting cylinder," IEICE Trans. Electron. (Japanese Edition), vol.J87-C, no.10, pp.754-767, Oct. 2004.

[15] T. Ida, T. Ishihara, and K. Goto, "Frequency-domain and time-domain novel uniform asymptotic solutions for scattered fields by an impedance cylinder and a dielectric cylinder," IEICE Trans. Electron., vol.E88-C, no.11, pp.2124-2135, Nov. 2005. DOI: 10.1093/ietele/e88-c.11.2124

[16] J. Sun and L.-W. Li, "Dispersion of waves over a PEC cylinder coated with two-layer lossy dielectric materials," IEEE Trans. Antennas Propagat., vol.55, no.3, pp.877-881, Mar. 2007. DOI: 10.1109/TAP.2007.891856

[17] G. Roqueta, L. Jofre, and M.Q. Feng, "Analysis of the electromagnetic signature of reinforced concrete structures for nondestructive evaluation of corrosion damage," IEEE Trans. Instrum. Meas., vol.61, no.4, pp.1090-1098, Apr. 2012. DOI: 10.1109/TIM.2011.2174106

[18] M. Nishimoto and Y. Naka, "Analysis of transient scattering by a metal cylinder covered with inhomogeneous lossy material for nondestructive testing," IEICE Trans. Electron., vol.E101-C, no.1, pp.44-47, Jan. 2018. DOI: 10.1587/transele.E101.C.44

[19] M. Nishimoto, B.P.A. Rohman, Y. Naka, and K. Ogata, "Corrosion state estimation of rebar in reinforced concrete using ultra-wideband radar," IEICE Trans. Electron. (Japanese Edition), vol.J104-C, no.11, pp.319-325, Nov. 2021. DOI: 10.14923/transelej.2021JCI0001

[20] Federal Communications Commission (FCC), ed., First report and order: Revision of part 15 of the commission's rules regarding ultra-wideband transmission systems, FCC 02-48, Washington, D.C., Apr. 2002.

[21] K. Hagiwara, K. Goto, S. Tokumaru, L. Okada, and Y. Takeno, "Novel time-domain asymptotic-numerical solutions for transient scattered electric field from a coated cylinder covered with a thick dielectric medium," IEICE Electron. Express, vol.14, no.5, 20170085, pp.1-10, Mar. 2017. DOI: 10.1587/elex.14.20170085

[22] T. Kawano and K. Goto, "Novel time-domain asymptotic-numerical solution for backward transient scattered magnetic field from a coated metal cylinder," IEICE Electron. Express, vol.18, no.2, 20200399, pp.1-6, Jan. 2021. DOI: 10.1587/elex.18.20200399

[23] T. Kawano and K. Goto, "Interpretation method of inversion phenomena on backward transient scattered field components by a coated metal cylinder," IEICE Trans. Electron., vol.E105-C, no.9, pp.389-397, Sept. 2022. DOI: 10.1587/transele.2021ECP5051

[24] K. Goto and T. Kawano, "A study on the polarization dependence of backward transient scattering by a two-dimensional coated conducting cylinder using the TD-SPT," Proc. ICEAA 2022, p.26, Cape Town, Sept. 2022. DOI: 10.1109/ICEAA49419.2022.9900030

[25] T. Kawano and K. Goto, "A novel time-domain asymptotic solution for a backward transient scattered electric field by a coated metal cylinder," Proc. ICEAA 2022, pp.27-30, Cape Town, Sept. 2022. DOI: 10.1109/ICEAA49419.2022.9899979

[26] K. Goto and T. Kawano, "An interpretation method on amplitude intensities for response waveforms of backward transient scattered field components by a 2-D coated metal cylinder," IEICE Trans. Electron., vol.E106-C, no.4, pp.118-126, Apr. 2023. DOI: 10.1587/transele.2022REP0001

[27] K. Goto, T. Kawano, M. Iwakiri, T. Kawakami, and K. Nakazawa, "Method for estimating scatterer information from the response waveform of a backward transient scattering field using TD-SPT," IEICE Trans. Electron., Aug. 2024. DOI: 10.1587/transele.2023ECP5040

[28] K. Goto, T. Kawano, H. Koriyama, M. Kato, and M. Iwakiri, "Estimation method of scatterer information using the response waveform of a backward transient scattered magnetic field by the TD-SPT ~ Case where source and observation points are located at same position ~," The Papers of Technical Meeting on Electromagnetic Theory, IEE Japan, EMT-22-51, pp.61-68, Jul. 2022.

[29] K. Goto, M. Iwakiri, T. Kawano, M. Kato, and H. Koriyama, "Estimation method of scatterer information using response waveforms of backward transient scattered magnetic fields by the TD-SPT ~ Applicable condition of the Estimation method ~," The 2022 IEICE Society Conference, CS-1-2, pp.S-2~S-3, Sept. 2022.

[30] M. Abramowitz and I.A. Stegun, eds., Handbook of Mathematical Functions, 10th ed., Dover, New York, 1972.

[31] E.O. Brigham, ed., The Fast Fourier Transform, Prentice-Hall, New Jersey, 1974.

Appendix A: Applicable Conditions of the Scatterer Information Estimation Method and Minimum Thickness of a Coating Medium Layer

First, the applicable condition of the scatterer information estimation method for the time in Section 4.3 is given by the following equation [27], [29]

$$t_2 \geq t_0 \tag{A·1}$$

where t_0 is a constant parameter of $s(t)$ in (1). The notation t_2 is the time required for a round trip through a coating medium layer of thickness h (see propagation path $Q_0 \rightarrow R \rightarrow Q_0$ in Fig. 2) and is expressed by the following equation using the speed of light c_2 in medium 2

$$t_2 = \frac{2h}{c_2},\ c_2 = \frac{1}{\sqrt{\varepsilon_2 \mu_0}} = \frac{c_0}{\sqrt{\varepsilon_{2r}}}. \tag{A·2}$$

Second, the applicable condition of the scatterer information estimation method for the thickness of a coating medium layer in Section 4.3 is given by the following equation [27], [29]

$$h \geq h_c \tag{A·3}$$

where h_c is the minimum thickness given by

$$h_c = \frac{t_0 c_2}{2} = \frac{t_0 c_0}{2\sqrt{\varepsilon_{2r}}}. \tag{A·4}$$

Appendix B: Time-Domain Saddle-Point Technique (TD-SPT) When a Line Source and an Observation Point are at the Same Location

As shown in Figs. 1 and 2, the TD-SPT for the z −direction component $y_j(\rho_0, \phi_0, \rho = \rho_0, \phi = \phi_0; t) = y_j(t), j = \mathrm{E}, \mathrm{H}$ of the backward transient scattering field when a line source $Q(\rho_0, \phi_0)$ and an observation point $P(\rho, \phi)$ are at the same location is given by the following formula, which employs the RGO series [28].

$$y_j(t) \sim y_{j,\,\text{TD-SPT}}(t) = \sum_{p=0}^{M_j} y_{j,\,\text{SPT},\,\text{RGO}_p}(t),\ j = \mathrm{E}, \mathrm{H} \tag{B· 1}$$

where $y_{j,\,\text{SPT},\,\text{RGO}_p}(t)$ is the RGO solution reflected p times at point R on a metal surface of inner radius $\rho = b$ shown in Fig. 2. The $y_{j,\,\text{SPT},\,\text{RGO}_p}(t)$ is given by

$$y_{j,\,\text{SPT},\,\text{RGO}_p}(t) = D(\omega_{s,\text{RGO}_p}) A_{j,\text{RGO}_p} \cdot \mathrm{Re}\left[\mathrm{erf}\beta(\omega_{s,\text{RGO}_p})\right] s\left(t - \frac{L_{\text{RGO}_p}}{c_1}\right) \quad \text{for } \frac{L_{\text{RGO}_p}}{c_1} \leq t \leq 2t_0 + \frac{L_{\text{RGO}_p}}{c_1} \tag{B·2}$$

where $D(\omega)$ and c_1 denote a common factor and the speed of light in a surrounding medium 1, respectively, and ω_{s,RGO_p} is a saddle point [28]. These factors are given by

$$D(\omega) = \sqrt{\frac{c_1}{8\pi\omega}} \exp(i\pi/4) \tag{B·3}$$

$$c_1 = \frac{1}{\sqrt{\varepsilon_1 \mu_0}} = \frac{c_0}{\sqrt{\varepsilon_{1r}}},\quad c_0 = \frac{1}{\sqrt{\varepsilon_0 \mu_0}} \tag{B·4}$$

$$\omega_{s,\text{RGO}_p} = \omega_0 - i\frac{1}{2d^2}\left(t - t_0 - \frac{L_{\text{RGO}_p}}{c_1}\right). \tag{B·5}$$

In (B·2), $\mathrm{erf}\, z$ and $s(t)$ denote the error function [30] in (4) and a pulse source in (1), respectively. The symbol $\beta(\omega)$ is defined in (3) and M_j is the number of truncated terms in the RGO series.

In $y_{j,\,\text{SPT},\,\text{RGO}_p}(t)$ in (B · 2), $D(\omega_{s,\text{RGO}_p}) A_{j,\text{RGO}_p}$ $\mathrm{Re}[\mathrm{erf}\beta(\omega_{s,\text{RGO}_p})]$ and L_{RGO_p} are the amplitude and distance functions of $y_{j,\,\text{SPT},\,\text{RGO}_p}(t)$, respectively.

B.1 Symbols $A_{j,\,\text{RGO}_0}$ and L_{RGO_0} of RGO_0 in (B·2)

The symbols $A_{j,\,\text{RGO}_0}$ and L_{RGO_0} of RGO_0 propagating along the path $Q \rightarrow Q_0 \rightarrow P$ (see Fig. 2), which is emitted at point Q and reflected at point Q_0 on a coating surface of outer radius $\rho = a$ before arriving at point P, are given by [28]

$$A_{j,\,\text{RGO}_0} = \hat{A}_{j,\,\text{RGO}_0} R_{j,\,11} \tag{B·6}$$

$$\hat{A}_{j,\,\text{RGO}_0} = \sqrt{\frac{a}{2L(a+L)}} \tag{B·7}$$

$$L_{\text{RGO}_0} = L_1 + L_2 = 2L \tag{B·8}$$

$$L_1 = \rho_0 - a = L = \mathrm{QQ}_0 \tag{B·9}$$

$$L_2 = \rho - a = L = \mathrm{Q}_0\mathrm{P}. \tag{B·10}$$

The symbol $\hat{A}_{j,\,\text{RGO}_0}$ is a divergence factor [2], [3] of

RGO_0 and L is a symbol for the same distance as $L_1(=\mathrm{QQ}_0)$ and $L_2(=\mathrm{Q}_0\mathrm{P})$ (see Fig. 2).

In (B·6), $R_{j,\,11}$ is a reflection coefficient on the convex side at point Q_0 and is defined as

$$R_{j,\,11}=\begin{cases}-\dfrac{\sqrt{\varepsilon_{2r}}-\sqrt{\varepsilon_{1r}}}{\sqrt{\varepsilon_{2r}}+\sqrt{\varepsilon_{1r}}} & \text{for } j=\mathrm{E}\\ +\dfrac{\sqrt{\varepsilon_{2r}}-\sqrt{\varepsilon_{1r}}}{\sqrt{\varepsilon_{2r}}+\sqrt{\varepsilon_{1r}}} & \text{for } j=\mathrm{H}\end{cases}. \tag{B·11}$$

B.2 Symbols $A_{j,\,\mathrm{RGO}_p}$ and L_{RGO_p} of $\mathrm{RGO}_p, p=1,2,\cdots,M_j$ in (B·2)

The symbols $A_{j,\,\mathrm{RGO}_p}$ and L_{RGO_p} of $\mathrm{RGO}_p, p=1,2,\cdots,M_j$ propagating along the path $\mathrm{Q}\rightarrow p(\mathrm{Q}_0\rightarrow\mathrm{R}\rightarrow)\mathrm{Q}_0\rightarrow\mathrm{P}$ (see Fig. 2), including the multiple reflection effect $p(\mathrm{Q}_0\rightarrow\mathrm{R}\rightarrow)\mathrm{Q}_0$ which is emitted at point Q and reflected p times at point R before arriving at point P, are given by [28]

$$A_{j,\,\mathrm{RGO}_p}=\hat{A}_{j,\,\mathrm{RGO}_p}T_{j,\,12}\left(R_{j,\,2}\right)^{p}\left(R_{j,\,22}\right)^{p-1}T_{j,\,21} \tag{B·12}$$

$$\hat{A}_{j,\,\mathrm{RGO}_p}=\sqrt{\frac{a}{2L(a+L)+D_p}} \tag{B·13}$$

$$D_p=p\frac{(a+L)^2(2h)}{a-h}\sqrt{\frac{\varepsilon_{1r}}{\varepsilon_{2r}}} \tag{B·14}$$

$$L_{\mathrm{RGO}_p}=2L+p\sqrt{\frac{\varepsilon_{2r}}{\varepsilon_{1r}}}(2h) \tag{B·15}$$

where $\hat{A}_{j,\,\mathrm{RGO}_p}$ represents a divergence factor of RGO_p and $T_{j,\,12}$ $(T_{j,\,21})$ expresses a transmission coefficient from medium 1 (medium 2) to medium 2 (medium 1) at point Q_0 (see Fig. 2), and are defined as follows

$$T_{j,\,12}=\begin{cases}\dfrac{2\sqrt{\varepsilon_{1r}}}{\sqrt{\varepsilon_{2r}}+\sqrt{\varepsilon_{1r}}} & \text{for } j=\mathrm{E}\\ \dfrac{2\sqrt{\varepsilon_{2r}}}{\sqrt{\varepsilon_{2r}}+\sqrt{\varepsilon_{1r}}} & \text{for } j=\mathrm{H}\end{cases} \tag{B·16}$$

$$T_{j,\,21}=\begin{cases}\dfrac{2\sqrt{\varepsilon_{2r}}}{\sqrt{\varepsilon_{2r}}+\sqrt{\varepsilon_{1r}}} & \text{for } j=\mathrm{E}\\ \dfrac{2\sqrt{\varepsilon_{1r}}}{\sqrt{\varepsilon_{2r}}+\sqrt{\varepsilon_{1r}}} & \text{for } j=\mathrm{H}\end{cases}. \tag{B·17}$$

In (B·12), $R_{j,\,2}$ and $R_{j,\,22}$ represent a reflection coefficient at point R and a reflection coefficient on the concave side at point Q_0 (see Fig. 2), respectively, and are defined as follows

$$R_{j,\,2}=\begin{cases}-1 & \text{for } j=\mathrm{E}\\ +1 & \text{for } j=\mathrm{H}\end{cases} \tag{B·18}$$

$$R_{j,\,22}=\begin{cases}+\dfrac{\sqrt{\varepsilon_{2r}}-\sqrt{\varepsilon_{1r}}}{\sqrt{\varepsilon_{2r}}+\sqrt{\varepsilon_{1r}}} & \text{for } j=\mathrm{E}\\ -\dfrac{\sqrt{\varepsilon_{2r}}-\sqrt{\varepsilon_{1r}}}{\sqrt{\varepsilon_{2r}}+\sqrt{\varepsilon_{1r}}} & \text{for } j=\mathrm{H}\end{cases}. \tag{B·19}$$

Keiji Goto received the B.E. and M.E. degrees (equivalents) from the National Defense Academy of Japan, Yokosuka, Japan, in 1984 and 1989, respectively, and the D.E. degree from the University of Tsukuba, Tsukuba, Japan, in 2001. From 1991 to 1996, he was a Researcher at the National Defense Academy of Japan. From 1996 to 2004, he was worked as a Researcher at the Japan Ground Self-Defense Force and at the Defense Agency (now the Ministry of Defense) in Japan. Since March 2004, he has been with the National Defense Academy of Japan, where he is currently a Professor. His current research interests include high-frequency scattering in the frequency and time domains. Dr. Goto received the Paper Presentation Award from the Institute of Electrical Engineers of Japan in 1993.

Toru Kawano received the B.E., M.E., and D.E. degrees in electrical engineering from Hosei University, Tokyo, Japan, in 1995, 1997, and 2001, respectively. Since April 2001, he has been with the National Defense Academy of Japan, where he is currently an Associate Professor. His current research interests include the scattering and propagation of electromagnetic waves, and antennas. Dr. Kawano received the Paper Presentation Award from the Institute of Electrical Engineers of Japan in 2008.

Ryohei Nakamura received the B.E., M.E., and D.E. degrees in information engineering from The University of Kitakyushu, Japan, in 2009, 2011, and 2014, respectively. In 2014, he was a research associate in the Department of Communication Engineering, National Defense Academy of Japan, and has been an Associate Professor in the same department since 2020. His major research interests include wireless communications, millimeter radio propagation, radar sensor systems, and network systems. He is a member of the IEICE and IEEE.